

1 **Technical note: Applicability of physics-based and machine-learning-based**
2 **algorithms of geostationary satellite in retrieving the diurnal cycle of cloud base**
3 **height**

4
5 Mengyuan Wang¹, Min Min^{1*}, Jun Li², Han Lin³, Yongen Liang¹, Binlong Chen²,
6 Zhigang Yao⁴, Na Xu², Miao Zhang²

7
8
9 ¹School of Atmospheric Sciences, Southern Marine Science and Engineering
10 Guangdong Laboratory (Zhuhai), and Guangdong Province Key Laboratory for
11 Climate Change and Natural Disaster Studies, Zhuhai 519082, China

12 ²Key Laboratory of Radiometric Calibration and Validation for Environmental
13 Satellites and Innovation Center for FengYun Meteorological Satellite (FYSIC),
14 National Satellite Meteorological Center (National Center for Space Weather), China
15 Meteorological Administration, Beijing 100081, China

16 ³Key Laboratory of Spatial Data Mining and Information Sharing of Ministry of
17 Education, National and Local Joint Engineering Research Center of Satellite
18 Geospatial Information Technology, Fuzhou University, Fuzhou 350108, China

19 ⁴Beijing Institute of Applied Meteorology, Beijing 100029, China

20
21
22
23 *Correspondence to:* Min Min (minm5@mail.sysu.edu.cn)

24
25
26
27
28
29
30
31
32
33

34 **Abstract.** Two groups of retrieval algorithms, physics-based and the other
35 machine-learning (ML) based, each consisting of two independent approaches, have
36 been developed to retrieve cloud base height (CBH) and its diurnal cycle from
37 Himawari-8 geostationary satellite observations. Validations have been conducted
38 using the joint CloudSat/CALIOP (Cloud-Aerosol Lidar with Orthogonal Polarization)
39 CBH products in 2017, ensuring independent assessments. Results show that the two
40 ML-based algorithms exhibit markedly superior performance (the optimal method is
41 with a correlation coefficient of $R > 0.91$ and an absolute bias of approximately 0.8
42 km) compared to the two physics-based algorithms. However, validations based on
43 CBH data from the ground-based lidar at the Lijiang station in Yunnan province and
44 the cloud radar at the Nanjiao station in Beijing, China, explicitly present
45 contradictory outcomes ($R < 0.60$). An identifiable issue arises with significant
46 underestimations in the retrieved CBH by both ML-based algorithms, leading to an
47 inability to capture the diurnal cycle characteristics of CBH. The strong consistence
48 observed between CBH derived from ML-based algorithms and the spaceborne active
49 sensors of CloudSat/CALIOP may be attributed to utilizing the same dataset for
50 training and validation, sourced from the CloudSat/CALIOP products. In contrast, the
51 CBH derived from the optimal physics-based algorithm demonstrates the good
52 agreement in diurnal variations of CBH with ground-based lidar/cloud radar
53 observations during the daytime (with an R value of approximately 0.7). Therefore,
54 the findings in this investigation from ground-based observations advocate for the
55 more reliable and adaptable nature of physics-based algorithms in retrieving CBH
56 from geostationary satellite measurements. Nevertheless, under ideal conditions, with
57 an ample dataset of spaceborne cloud profiling radar observations encompassing the
58 entire day for training purposes, the ML-based algorithms may hold promise in still
59 delivering accurate CBH outputs.

60 **Key words:** Geostationary meteorological satellite; cloud base height; physics-based
61 algorithm; machine learning.

62

63 **1 Introduction**

64 Clouds, comprising visible aggregates like atmospheric water droplets,
65 supercooled water droplets, ice crystals, etc., cover roughly 70% of the Earth's surface
66 (Stubenrauch et al., 2013). They play a pivotal role in global climate change, the
67 hydrometeor cycle, aviation safety, and serve as a primary focus in weather
68 forecasting and climate research, particularly storm clouds (Hansen, 2007; Hartmann
69 and Larson, 2002). From advanced geostationary (GEO) and polar-orbiting (LEO,
70 low earth orbit) satellite imagers, various measurable cloud properties, such as cloud
71 fraction, cloud phase, cloud top height (CTH), and cloud optical thickness (D_{COT}), are
72 routinely retrieved. However, the high-quality cloud geometric height (CGH) and
73 cloud base height (CBH), a fundamental macro physical parameter delineating the
74 vertical distribution of clouds, remains relatively understudied and underreported.
75 Nonetheless, for boundary-layer clouds, the cloud base height stands as a critical
76 parameter depending on other cloud-controlling variables. These variables encompass
77 the cloud base temperature (Zhu et al., 2014), cloud base vertical velocity (Zheng et
78 al., 2020), activation of CCN (Cloud Condensation Nuclei) at the cloud base
79 (Rosenfeld et al., 2016; Miller et al., 2023), and the cloud-surface decoupling state
80 (Su et al., 2022). These factors significantly impact convective cloud development
81 and ultimately the climate. As well known, there are distinct diurnal cycle
82 characteristics of clouds in different regions across the globe (Li et al., 2022). These
83 diurnal cycle characteristics primarily stem from the daily solar energy cycle absorbed
84 by both the atmosphere and Earth's surface. Besides, vertical atmospheric motions are
85 shaped by imbalances in atmospheric heating and surface configurations, also leading
86 to a range of cloud movements and structures (Miller et al., 2018). Cloud base plays a
87 pivotal role in weather and climate processes. It is critical for predicting fog and
88 cloud-related visibility issues important in aviation and weather forecasting. For
89 instance, lower cloud bases often lead to more intense rainfall. In climate modeling,
90 CBH is integral for accurate long-term weather predictions and understanding the
91 radiative balance of the Earth, which influences global temperatures (Zheng and
92 Rosenfeld, 2015). Hence, the accurate determination of CBH and its diurnal cycle
93 with high spatiotemporal resolution becomes very important, necessitating
94 comprehensive investigations (Viúdez-Mora et al., 2015; Wang et al., 2020). Such

95 efforts can provide deeper insights into potential ramifications of clouds on radiation
96 equilibrium and global climate systems.

97 However, as one of the most crucial cloud physical parameters in atmospheric
98 physics, the CBH poses challenges in terms of measurement or estimation from space.
99 Presently, the primary methods for measuring CBH rely on ground-based
100 observations, utilizing tools such as sounding balloons, Mie-scattering lidars,
101 stereo-imaging cloud-height detection technologies, and cloud probe sensors
102 (Forsythe et al., 2000; Hirsch et al., 2011; Seaman et al., 2017; Zhang et al., 2018;
103 Zhou et al., 2019; Zhou et al., 2024). While *in-situ* ground-based observation methods
104 offer highly accurate, reliable, and timely continuous CBH results, they are
105 constrained by localized observation coverage and the sparse distribution of
106 observation sites (Aydin and Singh, 2004). In recent decades, with the rapid
107 advancement of meteorological satellite observation technology, spaceborne
108 observing methods have emerged that provide global cloud observations with high
109 spatiotemporal resolution compared to conventional ground-based remote sensing
110 methods. In this realm, satellite remote sensing techniques for measuring CBH fall
111 primarily into two categories: active and passive methods. Advanced active remote
112 sensing technologies like CloudSat (Stephens et al., 2002) and Cloud-Aerosol Lidar
113 and Infrared Pathfinder Satellite Observation (CALIPSO) (Winker et al., 2009) in the
114 National Aeronautics and Space Administration (NASA) A-Train (Afternoon-Train)
115 series (Stephens et al., 2002) can capture global cloud profiles, including CBH, with
116 high quality by detecting unique return signals from cloud layers using onboard active
117 millimeter wave radar or lidar. However, their viewing footprints are limited along the
118 nadir of the orbit, implying that observation coverage remains confined primarily to a
119 horizontal scale (Min et al., 2022; Lu et al., 2021).

120 In addition to active remote sensing methods, satellite-based passive remote
121 sensing technologies can also play an important role in estimating CBH (Meerkötter
122 and Bugliaro, 2009; Lu et al., 2021). The physics-based principles and retrieval
123 methods for CTH have reached maturity and are now widely employed in satellite
124 passive remote sensing field (Heidinger and Pavolonis, 2009; Wang et al., 2022).
125 However, the corresponding physical principles or methods for measuring CBH using
126 satellite passive imager measurements are still not entirely clear and unified
127 (Heidinger et al., 2019; Min et al., 2020). A recent study by (Yang et al., 2021)
128 utilized oxygen A-band data observed by the Orbiting Carbon Observatory 2 (OCO-2)

129 to retrieve single-layer marine liquid CBH. These passive space-based remote sensing
130 methods aforementioned, such as satellite imagery, play a key role in retrieving CBH.
131 In terms of detection principles, the first method involves the extrapolation technique
132 for retrieving CBH for clouds of the same type. For instance, (Wang et al., 2012)
133 proposed a method to extrapolate CBH from CloudSat using spatiotemporally
134 matched MODIS (Moderate Resolution Imaging Spectroradiometer) cloud
135 classification data (Baum et al., 2012; Platnick et al., 2017). The second
136 physics-based retrieval method first approximates the cloud geometric thickness using
137 its optical thickness. It then employs the previously derived CTH product to compute
138 the corresponding CBH using the respective NOAA (National Oceanic and
139 Atmospheric Administration) SNPP/VIIRS (Suomi National Polar-orbiting
140 Partnership/Visible Infrared Imaging Radiometer Suite) products (Noh et al., 2017).
141 Hutchison et al. (2002 and 2006) also formulated an empirical algorithm that
142 estimates both cloud geometric thickness (CGT) and CBH. This algorithm relies on
143 statistical analyses derived from MODIS D_{COT} and cloud liquid water path products
144 (Hutchison et al., 2006; Hutchison, 2002).

145 Machine learning (ML) has proven to be highly effective in addressing nonlinear
146 problems within remote sensing and meteorology fields, such as precipitation
147 estimation and CTH retrieval (Min et al., 2020; HåKansson et al., 2018; Kühnlein et
148 al., 2014). In recent years, several studies have leveraged ML-based algorithms to
149 retrieve CBH, establishing nonlinear connections between CBH and GEO satellite
150 observations. For instance, Tan et al. (2020) integrated CTH and cloud optical
151 properties products from Fengyun-4A (FY-4A) GEO satellite with spatiotemporally
152 matched CBH data from CALIPSO/CloudSat. They developed a random forest (RF)
153 model for CBH retrieval. Similarly, Lin et al. (2022) constructed a gradient boosted
154 regression tree (GBRT) model using U.S. new-generation Geostationary Operational
155 Environmental Satellites-R Series (GOES-R) Advanced Baseline Imager (ABI) level
156 1B radiance data and the ERA5 (the fifth generation ECMWF) reanalysis dataset
157 (<https://cds.climate.copernicus.eu/cdsapp#!/search?type=dataset>). They employed
158 CALIPSO CBH data as labels to achieve single-layer CBH retrievals. Notably, the
159 CBH quality of ML-based algorithms was found to surpass that of physics-based
160 algorithms (Lin et al., 2022). Moreover, Tana et al. (2023) utilized Himawari-8 data
161 and the RF algorithm to develop a novel CBH algorithm, achieving a similar high
162 correlation coefficient (R) of 0.92 and a low root mean square error (RMSE) of 1.17

163 km compared with CloudSat/CALISPO data.

164 However, these former studies did not discuss whether both physics-based and
165 ML-based algorithms of GEO satellite could retrieve the diurnal cycle of CBH well.
166 This gap in research could be mainly attributed to potential influences from the fixed
167 LEO satellite (with active radar or lidar) passing time in the previous CBH retrieval
168 model (Lin et al., 2022). The diurnal cycles of CBH have not been well investigated
169 in both GEO and LEO remote sensing research. Hence, it is crucial to thoroughly
170 investigate the diurnal cycle features of CBH derived from GEO satellite
171 measurements by comparing them with ground-based radar and lidar observations
172 (Min and Zhang, 2014; Warren and Eastman, 2014). In this study, we aim to assess
173 the applicability and feasibility of both physics-based and ML-based algorithms of
174 GEO satellites in capturing the diurnal cycle characteristics of CBH.

175 The subsequent sections of this paper are structured as follows. Section 2
176 provides a concise overview of the data employed in this study. Following that,
177 section 3 introduces the four distinct physics/ML-based CBH retrieval algorithms. In
178 section 4, the CBH results obtained from these four algorithms are analyzed, and
179 comparisons are drawn with spatiotemporally matched CBHs from ground-based
180 cloud radar and lidar. Finally, section 5 encapsulates the primary conclusions and new
181 findings derived from this study.

182 **2 Data**

183 In this study, observations from the Himawari-8 (H8) Advanced Himawari
184 Imager (AHI) are utilized for the retrieval of high spatiotemporal resolution CBH.
185 Launched successfully by the Japan Meteorological Administration on October 7,
186 2014, the H8 geostationary satellite is positioned at 140.7°E. The AHI onboard H8
187 encompasses 16 spectral bands ranging from 0.47 μm to 13.3 μm , featuring spatial
188 resolutions of 0.5–2 km. This includes 3 visible (VIS) bands at 0.5–1 km, 3
189 near-infrared (NIR) bands at 1–2 km, and 10 infrared (IR) bands at 2 km. The
190 H8/AHI can scan a full disk area within 10 minutes, two specific areas within 2.5
191 minutes, a designated area within 2.5 minutes, and two landmark areas within 0.5
192 minutes (Iwabuchi et al., 2018). Its enhanced temporal resolution and observation
193 frequency facilitate the tracking of rapidly changing weather systems, enabling the
194 accurate determination of quantitative atmospheric parameters (Bessho et al., 2016).

195 Operational H8/AHI Level-1B data, accessible from July 7, 2015, are freely
196 available on the satellite product homepage of the Japan Aerospace Exploration
197 Agency (Letu et al., 2019). The Level-2 cloud products utilized in this study,
198 including cloud mask (CLM), CTH, cloud effective particle radius (CER or R_{eff}), and
199 D_{COT} , are generated by the Fengyun satellite science product algorithm testbed
200 (FYGAT) (Wang et al., 2019; Min et al., 2017) of the China Meteorological
201 Administration (CMA) for various applications. According to previous CALIPSO
202 validations (Min et al., 2020), the absolute bias of cloud top height retrieved by the
203 H8 satellite is approximately 3 km, with an absolute bias of 1 to 2 km for samples
204 below 5 km. The accuracy of CTH is crucial for estimating CBH in the subsequent
205 algorithm. It is important to note that certain crucial preliminary cloud products, such
206 as CLM, have been validated in prior studies (Wang et al., 2019; Liang et al., 2023).
207 Nevertheless, before initiating CBH retrieval, it is imperative to validate the H8/AHI
208 cloud optical and microphysical products from the FYGAT retrieval system. This
209 validation has been carried out by using analogous MODIS Level-2 cloud products as
210 a reference. Additional details regarding the validation of cloud products are provided
211 in the Appendix A section.

212 In addition to the H8/AHI Level-1/2 data, the Global Forecast System (GFS)
213 numerical weather prediction (NWP) data are employed for CBH retrieval in this
214 study. The variables include land/sea surface temperature and the vertical profiles of
215 temperature, humidity, and pressure. Operated by the U.S. NOAA (Kalnay et al.,
216 1996), the GFS serves as a global and advanced NWP system. The operational GFS
217 system routinely delivers global high-quality and gridded NWP data at 3-hour
218 intervals, with four different initial forecast times per day (00:00, 06:00, 12:00, and
219 18:00 UTC). The three-dimensional NWP data cover the Earth in a $0.5^{\circ} \times 0.5^{\circ}$ grid
220 interval and resolve the atmosphere with 26 vertical levels from the surface (1000 hPa)
221 up to the top of the atmosphere (10 hPa).

222 As previously mentioned, the official MODIS Collection-6.1 Level-2 cloud
223 product Climate Data Records (Platnick et al., 2017) are utilized in this study to
224 validate the H8/AHI cloud products (CTH, CER, and D_{COT}) generated by the FYGAT
225 system. High-quality, long-term series MODIS data is often used as a validation
226 reference to evaluate the products of new satellites. MODIS sensors are onboard
227 NASA Terra and Aqua polar-orbiting satellites. Terra functions as the morning
228 satellite, passing through the equator from north to south at approximately 10:30 local

229 time, while Aqua serves as the afternoon satellite, traversing the equator from south to
230 north at around 13:30 local time. As a successor to the NOAA Advanced Very High
231 Resolution Radiometer (AVHRR), MODIS features 36 independent spectral bands
232 and a broad spectral range from 0.4 μm (VIS) to 14.4 μm (IR), with a scanning width
233 of 2330 km and spatial resolutions ranging from 0.25 to 1.0 km. Recent studies
234 (Baum et al., 2012; Platnick et al., 2017) have highlighted significant improvements
235 and collective changes in cloud top, optical, and microphysical properties from
236 Collection-5 to Collection-6.

237 In addition to the passive spaceborne imaging sensors mentioned above, the
238 CloudSat satellite , equipped with a 94-GHz active cloud profiling radar (CPR), holds
239 the distinction of being the first sun-synchronous orbit satellite specifically designed
240 to observe global cloud vertical structures and properties. It is part of the A-Train
241 series of satellites, akin to the Aqua satellite, launched and operated by NASA
242 (Heymsfield et al., 2008). CALIPSO is another polar-orbiting satellite within the
243 A-Train constellation, sharing an orbit with CloudSat and trailing it by a mere 10–15
244 seconds. CALIPSO is the first satellite equipped with an active dual-channel CALIOP
245 at 532 and 1064 nm bands (Hunt et al., 2009). Both CloudSat and CALIPSO possess
246 notable advantages over passive spaceborne sensors due to the 94-GHz radar of
247 CloudSat and the joint return signals of lidar and radar on CALIPSO. These features
248 enhance their sensitivity to optically thin cloud layers and ensure strong penetration
249 capability, resulting in more accurate CTH and CBH detections compared to passive
250 spaceborne sensors (CAL_LID_L2_05kmCLay-Standard-V4-10). The joint cloud
251 type products of 2B-CLDCLASS-LIDAR, derived from both CloudSat and CALIPSO
252 measurements, offer a comprehensive description of cloud vertical structure
253 characteristics, cloud type, CTH, CBH, etc. The time interval between each profile in
254 this product is approximately 3.1 seconds, and the horizontal resolution is 2.5 km
255 (along track) \times 1.4 km (cross-track). Each profile is divided into 125 layers with a
256 240-m vertical interval. For more details on 2B-CLDCLASS-LIDAR products, please
257 refer to the CloudSat official product manual (Sassen and Wang, 2008). In this study,
258 we consider the lowest effective cloud base height from the joint CloudSat/CALIOP
259 data as the true values for training and validation. Please note that for this study, we
260 utilized one-year H8/AHI data and matched it with the joint CloudSat/CALIOP data
261 from January 1 to December 31 of 2017.

262 **3 Physics/machine-learning based cloud base height algorithms**

263 **3.1 GEO cloud base height retrieval algorithm from the interface data processing**
264 **segment of the Visible Infrared Imaging Radiometer Suite**

265 The Joint Polar Satellite System (JPSS) program is a collaborative effort between
266 NASA and NOAA. The operational CBH retrieval algorithm, part of the 30
267 Environmental Data Records (EDR) of JPSS, can be implemented operationally
268 through the Interface Data Processing Segment (IDPS) (Baker, 2011). In this study,
269 our geostationary satellite CBH retrieval algorithm aligns with the IDPS CBH
270 algorithm developed by (Baker, 2011). Utilizing the geostationary H8/AHI cloud
271 products discussed earlier, this new GEO CBH retrieval algorithm is succinctly
272 outlined below. It is important to note that multilayer cloud scenes remain a challenge
273 for retrieving both CTH and CBH, especially when considering the column-integrated
274 cloud water path (CWP) used in physics-based algorithms (Noh et al., 2017). In this
275 study, we will simplify the scenario by assuming a single-layer cloud for all
276 algorithms.

277 The new GEO IDPS CBH algorithm initiates the process by first retrieving the
278 CGT from bottom to top. Subsequently, CGT is subtracted from the corresponding
279 CTH to calculate CBH ($CBH = CTH - CGT$). The algorithm is divided into two
280 independent executable modules based on cloud phase, distinguishing between liquid
281 water and ice clouds. CBH of water cloud retrieval requires D_{COT} and CER as inputs.
282 For ice clouds, an empirical equation is employed for CBH retrieval. However, the
283 standard deviations of error in IDPS CBH for individual granules often exceed the
284 JPSS VIIRS minimum uncertainty requirement of $\pm 2\text{km}$ (Noh et al., 2017). For a
285 more comprehensive understanding of this CBH algorithm, please refer to the IDPS
286 algorithm documentation (Baker, 2011). Note that, similar to previous studies on
287 cloud retrieval (Noh et al., 2017; Platnick et al., 2017), this investigation also assumes
288 a single-layer cloud for all CBH algorithms, due to the challenges associated with
289 determining multilayer cloud structures.

290 **3.2 GEO cloud base height retrieval algorithm implemented in the Clouds from**
291 **Advanced Very High Resolution Radiometer Extended system**

292 As mentioned above, the accuracy of the GEO IDPS algorithm is highly
293 dependent on the initial input parameters such as cloud phase, D_{COT} and R_{eff} , which

may introduce some uncertainties in the final retrieval results. In contrast, another statistically-based algorithm is proposed and implemented here, which is named the GEO CLAVR-x (Clouds from AVHRR Extended, NOAA's operational cloud processing system for the AVHRR) CBH algorithm (Noh et al., 2017), and it mainly refers to NOAA AWG CBH algorithm (ACBA) (Noh et al., 2022). Previous studies have also demonstrated a R of 0.569 and a RMSE of 2.3 km for the JPSS VIIRS CLAVR-x CBH algorithm. It is anticipated that this algorithm will also be employed for the NOAA GOES-R geostationary satellite imager (Noh et al., 2017; Seaman et al., 2017).

Similar to the GEO IDPS CBH retrieval algorithm mentioned earlier, the GEO CLAVR-x CBH retrieval algorithm also initially obtains CGT and CTH, subsequently calculating CBH by subtracting CGT from CTH (CTH–CGT). However, the specific calculation method for the CGT value differs. This algorithm is suitable for single-layer and the topmost layer of multi-layer clouds, computing CBH using the CTH at the top layer of the cloud. In comparison with the former GEO IDPS CBH algorithm, the GEO CLAVR-x CBH algorithm considers two additional cloud types: deep convection clouds and thin cirrus clouds. For more details on this CLAVR-x CBH algorithm, please refer to the original algorithm documentation (Noh et al., 2017).

3.3 Random-forest-based cloud base height estimation algorithm

RF, one of the most significant ML algorithms, was initially proposed and developed by (Breiman, 2001). It is widely employed to address classification and regression problems based on the law of large numbers. The RF method is well-suited for capturing complex or nonlinear relationships between predictors and predictands.

In this study, two distinct ML-based GEO CBH algorithms, namely VIS+IR and IR-single (only uses observations of H8/AHI IR channels), are devised to retrieve or predict the CBH using different sets of predictors. The RF training of the chosen predictors is formulated as follows:

$$\text{CBH} = \text{RF}_{\text{reg}}[x_1, x_2, \dots, x_n], \quad (1)$$

where RF_{reg} denotes the regression RF model, and x_i represents the i th predictor. The selected predictors from H8/AHI for both the VIS+IR and IR RF model training and prediction are detailed in Table 1, mainly referencing Min et al. (2020) and Tan et al. (2020). The VIS+IR algorithm retrieves CBH using NWP data (atmospheric

327 temperature and altitude profiles, total precipitable water (TPW), surface temperature),
328 surface elevation, air mass 1 (air mass 1=1/cos(view zenith angle)), and air mass 2 (air
329 mass 2=1/cos(solar zenith angle)). The rationale for choosing air mass and TPW is
330 their ability to account for the potential absorption effect of water vapor along the
331 satellite viewing angle. The predictors in CBH retrieval also include the IR band
332 Brightness Temperature (BT) and VIS band reflectance. The IR-single algorithm
333 selects the same GFS NWP data as the VIS+IR algorithm but employs only view
334 zenith angles and azimuth angles.

335 To optimize the RF prediction model, the hyperparameters of the RF model are
336 tuned individually. The parameters and their dynamic ranges involved in tuning the
337 RF prediction models include the number of trees [100, 200, 300, 400, 500], the
338 maximum depth of trees [10, 20, 30, 40, 50], the minimum number of samples
339 required to split an internal node [2, 4, 6, 8, 10], and the minimum number of samples
340 required to be at a leaf node [1, 3, 5, 7, 9]. In this study, we set the smallest number of
341 trees in the forest to 100 and the maximum depth of the tree to 40.

342 **3.4 Evaluation method**

343 The performance of RF models and physics-based methods will be assessed using
344 mean absolute error (MAE), mean bias error (MBE), RMSE, R, and standard
345 deviation (STD) scores using the testing dataset. These scores mentioned above are
346 used to understand different aspects of the predictive performance of model: MAE
347 and RMSE provide insights into the average error magnitude, MBE indicates bias in
348 the predictions, R evaluates the linear association between observed and predicted
349 values, and STD assesses the variability of the predictions. In the RF IR-single
350 algorithm, 581,783 matching points are selected from H8/AHI and CloudSat data for
351 2017. Seventy percent of these points are randomly assigned to the training dataset,
352 and the remainder serves as the testing dataset. For the RF VIS+IR algorithm, a total
353 of 418,241 matching points are chosen, with 70% randomly allocated to the training
354 set. Note that the reduced data amount is because only daytime data can be used for
355 the VIS+IR method training. It's important to note that the two training datasets in
356 CloudSat will also be used to verify the CBHs obtained by cloud radar and lidar. The
357 statistical formulas for evaluation are as follows:

358
$$\text{MAE} = \frac{1}{n} \sum_{i=1}^n |y_i - x_i|, \quad (2)$$

359 $MBE = \frac{1}{n} \sum_{i=1}^n (y_i - x_i),$ (3)

360 $RMSE = \sqrt{\frac{1}{n} \sum_{i=1}^n (y_i - x_i)^2},$ (4)

361 $R = \frac{\sum_{i=1}^n (y_i - \bar{y})(x_i - \bar{x})}{\sqrt{\sum_{i=1}^n (y_i - \bar{y})^2} \sqrt{\sum_{i=1}^n (x_i - \bar{x})^2}},$ (5)

362 $STD = \sqrt{\frac{1}{n-1} \sum_{i=1}^n (x_i - \bar{x})^2},$ (6)

363 where n is the sample number, y_i is the i th CBH retrieval result, and x_i is the i th joint
364 CloudSat/CALIOP CBH product.

365 Since the two RF models (VIS+IR and IR-single) select 230 typical variables to
366 fit CBHs, the importance scores of these predictors in the two ML-based algorithms
367 are ranked for better optimization. In a RF model, feature importance indicates how
368 much each input variable contributes to the model's predictive accuracy by measuring
369 the decrease in impurity or error when the feature is used to split data (Gregorutti et
370 al., 2017). In the VIS+IR model, the top-ranked predictors are CTH and cloud top
371 temperature (CTT) from the H8/AHI Level-2 product (see Fig. B1 in Appendix B). It
372 is important to note that D_{COT} is a crucial and sensitive factor for these ML-based
373 algorithms. Retrieving CBH samples with relatively low D_{COT} remains challenging
374 due to the low signal-to-noise ratio when D_{COT} is low (Lin et al., 2022). To address
375 this issue, samples with D_{COT} less than 1.6 are filtered in the VIS+IR model, and
376 samples with relatively large BTs at Channel-14 are filtered in the IR-single model.
377 This filtering process significantly improves the R value from 0.869 to 0.922 in the
378 VIS+IR model and from 0.868 to 0.911 in the IR-single model. For more details on
379 the algorithm optimization, please refer to Appendix B.

380 In this study, the H8/AHI satellite CBH data retrieved by the four algorithms
381 mentioned before are matched spatiotemporally with the 2B-CLDCLASS-LIDAR
382 cloud product from joint CloudSat/CALIPSO observations in 2017. In this process,
383 the nearest distance matching method is employed, ensuring that collocating the
384 closest points and the observation time difference between the CloudSat/CALIPSO
385 observation point and the matched Himwari-8 data is less than 5 minutes (Noh et al.,
386 2017). As in earlier study (Min et al., 2020), we also used 70% of the matched data
387 for training and 30% of an independent sample for validation. Figure 1 displays a
388 comparison of CBH results over the full disk at 02:00 UTC on January 1, 2017,
389 retrieved by the GEO IDPS algorithm, the GEO CLAVR-x algorithm, the RF VIS+IR

algorithm, and the RF IR-single algorithm for all cloud conditions including single and multilayer cloud scenes. A similar distribution pattern and magnitude of CBHs retrieved by these four independent algorithms can be observed in Figure 1. However, notable differences exist between physics-based and ML-based algorithms. Further comparisons are conducted and analyzed with spaceborne and ground-based lidar and radar observations in the subsequent sections of this study.

396

397 **4 Results and Discussions**

398 **4.1 Comparisons with the joint CloudSat/CALIPSO cloud base height product**

399 **4.1.1 Joint scatter plots**

400 Figure 2 presents the density scatter plot of the CBHs retrieved from the GEO
401 IDPS and GEO CLAVR-x algorithms compared with the CBHs from the joint
402 CloudSat/CALIPSO product, along with the related scores of MAE, MBE, RMSE,
403 and R calculated and labeled in each panel. The calculated R exceeds the 95%
404 significance level ($p < 0.05$). For the GEO IDPS algorithm, the R is 0.62, the MAE is
405 1.826 km, and the MBE and RMSE are -0.232 and 2.642 km (Fig. 2a). In comparison,
406 (Seaman et al., 2017) compared the operational VIIRS CBH product retrieved by the
407 similar SNPP/VIIRS IDPS algorithm with the CloudSat CBH results. In their results,
408 the R is 0.569, and the RMSE is 2.3 km. For the new GEO CLAVR-x algorithm (Fig.
409 2b), the R is 0.647, and the RMSE is 2.91 km. The larger RMSE from two
410 independent physics-based CBH algorithms demonstrate a slightly poorer
411 performance and precision of these retrieval algorithms for GEO satellites.
412 Particularly, the larger RMSEs (2.642 and 2.91 km) indicate weaker stabilities of the
413 GEO IDPS and CLAVR-x CBH algorithms, compared with VIIRS CBH product
414 (Seaman et al., 2017). In this figure, more samples can be found near the 1:1 line,
415 implying the good quality of retrieved CBHs. However, in stark contrast, quite a
416 number of CBH samples retrieved by both GEO IDPS and GEO CLAVR-x
417 algorithms (compared with the official VIIRS CBH product) fall below 1.0 km,
418 indicating relatively large errors when compared with the joint CloudSat/CALIPSO
419 CBH product. Moreover, Figure 2 reveals that relatively large errors are also found in
420 the CBHs lower than 2 km for the four independent algorithms, primarily caused by
421 the weak penetration ability of VIS or IR bands on thick and low clouds.

422 Referring to the joint CloudSat/CALIPSO CBH product, Figures 2c and 2d
423 present the validations of the CBH results retrieved from two ML-based algorithms
424 using the VIS+IR (only retrieving the CBH during the daytime) and IR-single models.
425 Figure 2c demonstrates better consistency of CBH between the VIS+IR model and the
426 joint CloudSat/CALIPSO product with $R = 0.905$, $MAE = 0.817$ km, $MBE = 0.425$
427 km, and $RMSE = 1.706$ km. Figure 2d also displays a relatively high R of 0.876 when
428 validating the IR-single model, with $MAE = 0.882$, $MBE = -0.445$, and $RMSE =$
429 1.995. Therefore, both VIS+IR and IR-single models can obtain high-quality CBH
430 retrieval results from geostationary imager measurements. In comparison, previous
431 studies also proposed similar ML-based algorithms for estimating CBH using FY-4A
432 satellite imager data. For example, (Tan et al., 2020) used the variables of CTH, D_{COT} ,
433 R_{eff} , cloud water path, longitude/latitude from FY-4A imager data to build the training
434 and prediction model and obtained CBH with $MAE = 1.29$ km and $R = 0.80$. In this
435 study, except CTH, the other Level-2 products and geolocation data
436 (longitude/latitude) used in (Tan et al., 2020) are abandoned, while the matched
437 atmospheric profile products (such as temperature and relative humidity) from NWP
438 data are added. These changes in ML-based model training and prediction lead to
439 more accurate CBH retrieval results. Note that, in accordance with the previous study
440 conducted by (Noh et al., 2017), we excluded CBH samples obtained from
441 CloudSat/CALIPSO that were smaller than 1 km in our comparisons. This exclusion
442 was primarily due to the presence of ground clutter contamination in the CloudSat
443 CPR data (Noh et al., 2017).

444 4.1.2 Test case

445 Figure 3 displays two cross-sections of CBH from various sources overlaid with
446 CloudSat radar reflectivity (unit: dBZ) for spatiotemporally matched cases. The
447 periods covered are from 03:16 to 04:55 UTC on January 13, 2017 (154.0°E–160.0°E;
448 40.56°S–53.39°S) and from 05:38 to 07:17 UTC on January 14, 2017 (107.1°E–
449 107.8°E; 8.35°N–11.57°N). The CloudSat radar reflectivity and joint
450 CloudSat/CALIPSO product provide insights into the vertical structure or distribution
451 of clouds and their corresponding CBHs. The results from the four GEO CBH
452 retrieval algorithms (GEO IDPS, GEO CLAVR-x, RF VIS+IR model, and RF
453 IR-single model) mentioned earlier are individually marked with different markers in
454 each panel. According to Figure 3a, the GEO IDPS algorithm faces challenges in
455 accurately retrieving CBHs for geometrically thicker cloud samples near 157°E.

456 Optically thick mid- and upper-level cloud layers may obscure lower-level cloud
457 layers. However, the CBH results retrieved by the GEO IDPS algorithm near 155°E
458 (in Fig. 3a) and 107.4°E (in Fig. 3b) align with the joint CloudSat/CALIPSO CBH
459 product. It is worth noting that the inconsistency observed between 107.2°E and
460 107.3°E in Figure 3b, specifically regarding the CBHs around 1 km obtained from
461 CloudSat/CALIPSO, can likely be attributed to ground clutter contamination in the
462 CloudSat CPR data (Noh et al., 2017). The GEO CLAVR-x algorithm achieves
463 improved CBH results compared to the GEO IDPS algorithm. It can even retrieve
464 CBHs for some thick cloud samples that are invalid when using the GEO IDPS
465 algorithm. However, the CBHs from the GEO CLAVR-x algorithm are noticeably
466 higher than those from the joint CloudSat/CALIPSO product. In contrast, the CBHs
467 from the two ML-based algorithms show substantially better results than those from
468 the other two physics-based algorithms. Particularly, the ML-based VIS+IR model
469 algorithm yields the best CBH results. However, compared with those from the two
470 physics-based algorithms, the CBHs from the two ML-based algorithms still exhibit a
471 significant error around 5 km.

472 **4.2 Comparisons with the ground-based lidar and cloud radar measurements**

473 Lidar actively emits lasers in different spectral bands into the air. When the laser
474 signal encounters cloud particles during transmission, a highly noticeable
475 backscattered signal is generated and received (Omar et al., 2009). The lidar return
476 signal is markedly distinct from atmospheric aerosol scattering signals and noise,
477 making CBH easily obtainable from the signal difference or mutation (Sharma et al.,
478 2016). In this study, continuous ground-based lidar data from the Twin Astronomy
479 Manor in Lijiang City, Yunnan Province, China (26.454°N, 100.0233°E, altitude =
480 3175 m) are used to evaluate the diurnal cycle characteristics of CBHs retrieved using
481 GEO satellite algorithms (Young and Vaughan, 2009). The geographical location and
482 photo of this station are shown in Figure 4.

483 4.2.1 Comparison of CBH retrievals from ground and satellite data

484 The ground-based lidar data at Lijiang station on December 6, 2018, and January
485 8, 2019, are selected for validation. In fact, this lidar was primarily used for the
486 calibration of ground-based lunar radiation instruments. During the two-month
487 observation period (from December of 2018 to January of 2019), it was always
488 operated only under clear sky conditions, resulting in the capture of cloud data on just

489 two days. These two days have been cloudy, with stratiform clouds at an altitude of
490 around 5 km and no precipitation occurring. The number of available and
491 spatiotemporally matched CBH sample points from ground-based lidar is 78 and 64
492 on December 6, 2018, and January 8, 2019, respectively. Figure 5a and 5b show the
493 point-to-point CBH comparisons between ground-based lidar and four GEO satellite
494 CBH algorithms on December 6, 2018, and January 8, 2019. It is worth noting that
495 the retrieved CBHs of the two physics-based algorithms on December 6, 2018, are in
496 good agreement with the reference values from the lidar measurements, and, in
497 particular, the GEO CLAVR-x algorithm can obtain better results. From the results on
498 January 8, 2019, more accurate diurnal cycle characteristics of CBHs are revealed by
499 the GEO CLAVR-x algorithm than by the GEO IDPS algorithm.

500 Compared with the CBHs measured by ground-based lidar, the statistics of the
501 results retrieved from the GEO IDPS algorithm are $R = 0.67$, $MAE = 3.093$ km, $MBE = 0.856$ km,
502 and $RMSE = 3.609$ km (Fig. 5c). However, for cloud samples with CBH
503 below 7.5 km, the GEO IDPS algorithm shows an obvious underestimation of CBH in
504 Figure 5c. For the GEO CLAVR-x algorithm, it can also be seen that the matched
505 samples mostly lie near the 1:1 line with $R = 0.773$ (the optimal CBH algorithm),
506 $MAE = 1.319$ km, $MBE = 0.222$ km, and $RMSE = 1.598$ km. In addition, this figure
507 also shows the CBH comparisons between the ML-based VIS+IR model/IR-single
508 model algorithms and the lidar measurements, revealing that the retrieved CBH
509 results from the ML-based VIS+IR model are better than those from the ML-based
510 IR-single model algorithm. The comparison results between the CBHs of the
511 ML-based VIS+IR model algorithm and the lidar measurements are around the 1:1
512 line, with smaller errors and $R = 0.599$. In contrast, the R between the CBHs of the
513 ML-based IR-single model algorithm and the lidar measurements is only 0.494, with a
514 relatively large error. By comparing the retrieved CBHs with the lidar measurements
515 at Lijiang station, it indicates that CBH results from two physics-based algorithms are
516 remarkably more accurate, particularly that the GEO CLAVR-x algorithm can well
517 capture diurnal variation of CBH.

518 To further assess the accuracy and quality of the diurnal cycle of CBHs retrieved
519 with these algorithms, CBHs from another ground-based cloud radar dataset covering
520 the entire year of 2017 are also collected and used in this study. The observational
521 instrument is a Ka-band (35 GHz) Doppler millimeter-wave cloud radar (MMCR)
522 located at the Beijing Nanjiao Weather Observatory (a typical urban observation site)

523 (39.81°N, 116.47°E, altitude = 32 m; see Fig. 4), performing continuous and routine
524 observations. The MMCR provides a specific vertical resolution of 30 m and a
525 temporal resolution of 1 minute for single profile detection, based on the radar
526 reflectivity factor. In a previous study (Zhou et al., 2019), products retrieved by this
527 MMCR were utilized to investigate the diurnal variations of CTH and CBH, and
528 comparisons were made between MMCR-derived CBHs and those derived from a
529 Vaisala CL51 ceilometer. The former study also found that the average R of CBHs
530 from different instruments reached up to 0.65. It is worth noting that the basic physics
531 principle for detecting cloud base height from both spaceborne cloud profiling radar
532 and ground-based cloud radar and lidar measurements is the same. All these
533 algorithms of detecting CBH are based on the manifest change of return signals
534 between CBH and the clear sky atmosphere in the vertical direction (Huo et al., 2019;
535 Ceccaldi et al., 2013). As well known, the diurnal variation of cloud base height is
536 primarily influenced by solar heating, causing the cloud base to rise in the morning
537 and reach its peak by midday. As the surface cools in the afternoon and evening, the
538 cloud base lowers, playing a crucial role in weather patterns and forecasting (Zheng et
539 al., 2020). Due to the density of points in the one-year time series, the point-to-point
540 CBH comparison results for the entire year are not displayed here (monthly results are
541 shown in the supplementary document), we only show 4 days results in the following
542 Figure 6. Therefore, it is essential to rigorously compare the ML-based algorithm with
543 ground-based observations to determine its ability to adapt to the daily variations in
544 cloud base height caused by natural factors. The joint spaceborne CloudSat/CALIPSO
545 detection might face limitations in penetrating extremely dense, optically thick, or
546 areas with heavy precipitation clouds. Hence, in comparison, the CBH values
547 gathered from ground-based lidar and cloud radar measurements are expected to be
548 more accurate than the data derived from spaceborne CloudSat/CALIPSO detection.

549 Similar to Figure 5, Figure 6 presents two sample groups of CBH results from the
550 cloud radar at Beijing Nanjiao station relative to the matched CBHs from the four
551 retrieval algorithms (GEO IDPS, GEO CLAVR-x, ML-based IR-single, ML-based
552 VIS+IR) on April 9–10 and July 26–28, 2017. Similar to the results at Lijiang station
553 discussed in Figure 5, we observe better and more robust performances in retrieving
554 diurnal cycle characteristics of CBH from the two physics-based CBH retrieval
555 algorithms. In contrast, more underestimated CBH samples are retrieved by the two
556 ML-based algorithms.

557 4.2.2 Diurnal cycle analysis of CBH retrieval accuracy

558 To further investigate the diurnal cycle characteristics of retrieved CBH from
559 GEO satellite imager measurements, Figure 7 presents box plots of the hourly CBH
560 errors (relative to the results of cloud radar at Beijing Nanjiao station) in 2017 from
561 the four different CBH retrieval algorithms. Remarkably, there are significant
562 underestimations of the CBHs retrieved from the two ML-based algorithms. The
563 ML-based VIS+IR method achieves relatively better results than the ML-based
564 IR-single method during the daytime. Comparing the two ML-based algorithms, the
565 errors of the IR-single model algorithm have a similar standard deviation (2.80 km) to
566 those of the VIS+IR model algorithm (2.69 km) during the daytime. For the IR-single
567 model algorithm, it can be applied during both daytime and nighttime, its nighttime
568 performance degrades slightly, with an averaged RMSE (3.88 km) higher than that of
569 daytime (3.56 km). The nighttime CBH of the IR-single model algorithm is the only
570 choice that should be used with discretion.

571 Figure 8 shows the comparisons of hourly MAE, MBE, RMSE, and R relative to
572 the CBHs from the cloud radar at Beijing Nanjiao station during daytime between
573 four retrieval algorithms in 2017. The RMSE of the two ML-based algorithms shows
574 stable diurnal variation. It is noted that all algorithms have lower R at sunrise, around
575 07:00 local time, which improve as the day progresses. However, the GEO CLAVR-x
576 algorithm stands out for its relatively higher and more stable in R and RMSE during
577 daytime.

578 Figure 9a displays scatter plots and relevant statistics of the CBHs retrieved from
579 the GEO IDPS algorithm against the CBHs from cloud radar. The CBHs from the
580 GEO IDPS algorithm align well with the matched CBHs from cloud radar at Beijing
581 Nanjiao station, with $R = 0.515$, $MAE = 2.078$ km, $MBE = 1.168$ km, and $RMSE =$
582 2.669 km. In Figure 9b, the GEO CLAVR-x algorithm shows better results with $R =$
583 0.573, $MAE = 2.059$ km, $MBE = -0.204$ km, and $RMSE = 2.601$ km. It is not
584 surprising that Figs. 8c and 8d reveal obvious underestimated CBH results from the
585 two ML-based CBH algorithms. Particularly, the CBH results from the ML-based
586 VIS+IR model algorithm concentrate in the range of 2.5 km to 5 km. Therefore,
587 Figure 5 to Figure 9 further substantiates the weak diurnal variations captured by
588 ML-based techniques, primarily attributed to the scarcity of comprehensive CBH
589 training samples throughout the entire day. Besides, although the two robust
590 physics-based algorithms of GEO IDPS and GEO CLAVR-x (the optimal one) can

591 retrieve high-quality CBHs from H8/AHI data, especially the diurnal cycle of CBH
592 during the daytime, they still struggle to retrieve CBHs below 1 km.

593 **5. Conclusions and discussion**

594 To explore and argue the optimal and most robust CBH retrieval algorithm from
595 geostationary satellite imager measurements, particularly focusing on capturing the
596 typical diurnal cycle characteristics of CBH, this study employs four different
597 retrieval algorithms (two physics-based and two ML-based algorithms). High
598 spatiotemporal resolution CBHs are retrieved using the H8/AHI data from 2017 and
599 2019. To assess the accuracies of the retrieved CBHs, point-to-point validations are
600 conducted using spatiotemporally matched CBHs from the joint CloudSat/CALIOP
601 product, as well as ground-based lidar and cloud radar observations in China. The
602 main findings and conclusions are outlined below.

603 Four independent CBH retrieval algorithms, namely physics-based GEO IDPS,
604 GEO CLAVR-x, ML-based VIS+IR, and ML-based IR-single, have been developed
605 and utilized to retrieve CBHs from GEO H8/AHI data under the assumption of single
606 layer cloud. The two physics-based algorithms utilize cloud top and optical property
607 products from AHI as input parameters to retrieve high spatiotemporal resolution
608 CBHs, with operations limited to daytime. In contrast, the ML-based VIS+IR model
609 and IR-single model algorithms use the matched joint CloudSat/CALIOP CBH
610 product as true values for building RF prediction models. Notably, the ML-based
611 IR-single algorithm, which relies solely on infrared band measurements, can retrieve
612 CBH during both day and night.

613 The accuracy of CBHs retrieved from the four independent algorithms is verified
614 using the joint CloudSat/CALIOP CBH products for the year 2017. The GEO IDPS
615 algorithm shows an R of 0.62 and an RMSE of 2.642 km. The GEO CLAVR-x
616 algorithm provides more accurate CBHs with an R of 0.647 and RMSE of 2.91 km.
617 After filtering samples with optical thickness less than 1.6 and brightness temperature
618 (at 11 μ m band) greater than 281 K, the ML-based VIS+IR and ML-based IR-single
619 algorithms achieve higher accuracy with an R(RMSE) of 0.922(1.214 km) and
620 0.911(1.415 km), respectively. This indicates strong agreement between the two
621 ML-based CBH algorithms and the CloudSat/CALIOP CBH product.

622 However, in stark contrast, the results from the physics-based algorithms (with R
623 and RMSE of 0.592/2.86 km) are superior to those from the ML-based algorithms
624 (with R and RMSE of 0.385/3.88 km) when compared with ground-based CBH
625 observations such as lidar and cloud radar. In the comparison with the cloud radar at
626 Beijing Nanjiao station in 2017, the R of the GEO CLAVR-x algorithm is 0.573,
627 while the R of the GEO IDPS algorithm is 0.515. Meanwhile, notable differences are
628 observed in the CBHs between both ML-based algorithms. Similar conclusions are
629 also evident in the 2-day comparisons at Yunnan Lijiang station.

630 The CBH results from the two ML-based algorithms ($R > 0.91$) can likely be
631 attributed to the use of the same training and validation dataset source as the joint
632 CloudSat/CALIOP product. However, this dataset has limited spatial coverage and
633 small temporal variation, potentially limiting the representativeness of the training
634 data. In contrast, the GEO CLAVR-x algorithm demonstrates the best performance
635 and highest accuracy in retrieving CBH from geostationary satellite data. Notably, its
636 results align well with those from ground-based lidar and cloud radar during the
637 daytime. However, both physics-based methods, utilizing CloudSat CPR data for
638 regression, struggle to accurately retrieve CBHs below 1 km, as the lowest 1 km
639 above ground level of this data is affected by ground clutter.

640 Additionally, despite utilizing the same physics principles in spaceborne and
641 ground-based lidar/radar CBH algorithms, the previous study (Thorsen et al., 2011)
642 has highlighted differences in profiles between them. Therefore, this factor induced
643 by detection principle could contribute to the relatively poorer results in CBH
644 retrieval by ML-based algorithms compared to ground-based lidar and radar. The
645 analysis and discussion above suggest that ML-based algorithms are constrained by
646 the size and representativeness of their datasets.

647 Ideally, we guess that including more spaceborne cloud profiling radars with
648 varying passing times (covering the entire day) in the training dataset could improve
649 the machine learning technique, potentially leading to a higher-quality CBH product
650 with more comprehensive observations. The CBH product using ML-based
651 algorithms should continue to be improved in future work. Particularly, exploring the
652 joint ML-physics-based method presents a promising direction, which can address the
653 complexities and challenges in retrieving cloud properties. By integrating established
654 physical relationships into ML models, we can potentially enhance the accuracy and
655 reliability of predictions. This approach not only leverages the strengths of both

656 physics-based models and data-driven techniques but also offers a pathway to more
657 robust and interpretable solutions in atmospheric sciences. At present, we will focus
658 on developing physics-based algorithms for cloud base height for the next generation
659 of geostationary meteorological satellites, to support the application of these products
660 in weather and climate domains.

661 Besides, at night, current GEO satellite imaging instruments encounter
662 challenges in accurately determining CBH due to limited or absent solar illumination.
663 Because it is unable to retrieve cloud optical depth in the visible band, the current
664 method faces limitations. However, there is potential for enhanced accuracy in
665 deriving cloud optical and microphysical properties, as well as CBH, by incorporating
666 the Day/Night Band (DNB) observations during nighttime in the future (Walther et al.,
667 2013).

668

669

670 *Data availability.* The authors would like to acknowledge NASA, JMA, Colorado
671 State University, and NOAA for freely providing the MODIS
672 (<https://ladsweb.modaps.eosdis.nasa.gov/search>), CloudSat/CALIOP
673 (<https://www.cloudsat.cira.colostate.edu/>), Himawari-8 (<ftp://ptree.jaxa.jp>), and GFS
674 NWP (<ftp://nomads.ncdc.noaa.gov/GFS/Grid4>) data online, respectively.

675

676

677 *Author contributions.* MM proposed the essential research idea. MW, MM, JL, HL,
678 BC, and YL performed the analysis and drafted the manuscript. ZY and NX provided
679 useful comments. All the authors contributed to the interpretation and discussion of
680 results and the revision of the manuscript.

681

682

683 *Competing interests.* The authors declare that they have no conflict of interest.

684

685

686 *Acknowledgements.* The authors would like to acknowledge NASA, JMA, University
687 of Colorado, and NOAA for freely providing satellite data online, respectively. The

688 authors thank NOAA, NASA, and their VIIRS algorithm working groups (AWG) for
689 freely providing the VIIRS cloud base height algorithm theoretical basic
690 documentations (ATBD). In addition, the authors appreciate the power computer tools
691 developed by the Python and scikit-learn groups (<http://scikit-learn.org>). Besides the
692 authors also thank Rundong Zhou and Pan Xia for drawing some pictures of this
693 manuscript. Last but not the least, the authors sincerely thank Prof. Yong Zhang and
694 Prof. Jianping Guo for freely providing cloud base height results retrieved by
695 ground-based cloud radar at Beijing Nanjiao station. This work was supported partly
696 by the Guangdong Major Project of Basic and Applied Basic Research (Grant
697 2020B0301030004), National Natural Science Foundation of China under Grants
698 42175086 and U2142201, FengYun Meteorological Satellite Innovation Foundation
699 under Grant FY-APP-ZX-2022.0207, the Innovation Group Project of Southern
700 Marine Science and Engineering Guangdong Laboratory (Zhuhai) (No.
701 SML2023SP208), and the Science and Technology Planning Project of Guangdong
702 Province (2023B1212060019). We would like to thank the editor and anonymous
703 reviewers for their thoughtful suggestions and comments.

704

705

706 **Appendix A**

707 Based on the previously discussed description of two physics-based cloud base
708 height (CBH) retrieval algorithms (GEO IDPS and GEO CLAVR-x retrieval
709 algorithms), cloud products such as cloud top height (CTH), effective particle radius
710 (R_{eff}), and cloud optical thickness (D_{COT}) will be utilized in both algorithms. To
711 validate the reliability of these cloud products derived from the Advanced Himawari
712 Imager (AHI) aboard the Himawari-8 (H8), a pixel-by-pixel comparison is conducted
713 with analogous MODIS Collection-6.1 Level-2 cloud products. Both Aqua and Terra
714 MODIS Level-2 cloud products (MOD06 and MYD06) are accessible for free
715 download from the MODIS official website. For verification purposes, the
716 corresponding Level-2 cloud products from January, April, July, and October of 2018
717 are chosen to assess CTH, D_{COT} , and R_{eff} retrieved by H8/AHI.

718 Figure S2 (in the supplementary document) shows the spatiotemporally matched

719 case comparisons of CTH, D_{COT} and R_{eff} from H8/AHI and Terra/MODIS (MYD06)
720 at 03:30 UTC on January 15, 2018. It can be seen that the CTH, D_{COT} and R_{eff} from
721 H8/AHI are in good agreement with the matched MODIS cloud products. However,
722 there are still some differences in R_{eff} at the regions near 35°N, 110°E in Figures S2d
723 and S2c. The underestimated R_{eff} values from H8/AHI relative to MODIS have been
724 reported in previous studies. (Letu et al., 2019) compared the ice cloud products
725 retrieved from AHI and MODIS, and concluded that the R_{eff} from both products differ
726 remarkably in the ice cloud region and the D_{COT} from them are roughly similar.
727 However, the D_{COT} from AHI data is higher in some areas. Looking again at the cloud
728 optical thickness that at the same time, the slight underestimation of H8/AHI D_{COT}
729 can be found in Figures S2e and S2f. Figure S3 (in the supplementary document)
730 shows another case at 02:10 UTC on January 15, 2018. Despite of the good
731 consistence between H8/AHI and MODIS cloud products, there are slight differences
732 in CTH in the area around 40°S–40.5°S, 100°E–110°E in Figs. S3a and S3b. Besides,
733 as shown in Figure S2, there are still underestimations in the R_{eff} of H8/AHI.

734 To further compare and validate these three H8/AHI cloud products, the
735 spatiotemporally matched samples from H8/AHI and Aqua/Terra MODIS in four
736 months of 2018 are counted within the three intervals of 0.1 km (CTH), 1.0 μm (R_{eff}),
737 and 1 (D_{COT}) in Figure S4 (in the supplementary document). The corresponding mean
738 absolute error, mean bias error, RMSE and R values are also calculated and marked in
739 each subfigure. As can be seen, the R of CTH is around 0.75 in all four months and is
740 close to 0.8 in August. The results of D_{COT} show the highest R , reaching above 0.8. In
741 contrast, the underestimation trend in R_{eff} is also shown in this figure. These different
742 consistencies between two satellite-retrieved cloud products may be attributed to: (1)
743 different spatiotemporal resolutions between H8/AHI and MODIS; (2) different
744 wavelength bands, bulk scattering model, and specific algorithm used for retrieving
745 cloud products; (3) different view zenith angle between GEO and low-earth-orbit
746 satellite platforms (Letu et al., 2019). In addition, other external factors such as
747 surface type also can affect the retrieval of cloud product. However, according to
748 Figure S4, the bulk of the analyzed samples are still around the 1:1 line, indicating the
749 good quality of H8/AHI cloud products.

750

751 Appendix B

752 The ML-based visible (VIS)+infrared (IR) model algorithm mentioned above

753 uses 230 typical variables (see Table 1) as model predictors, and the importance
754 scores of top-30 predictors are ranked in Figure S5 (in the supplementary document).
755 It can be seen that the most important variables are CTH and CTT, and D_{COT} is an
756 important or sensitive factor affecting these two quantities. A sensitivity test is also
757 performed to further investigate the potential influence of D_{COT} on the CBH retrieval
758 by the VIS+IR model (see Table S1 in the supplementary document). From Figure
759 S7a, we find that the samples with D_{COT} lower than 5 cause the relatively large CBH
760 errors compared with the matched CBHs from the joint CALIPSO (Cloud-Aerosol
761 Lidar and Infrared Pathfinder Satellite Observation)/CloudSat product.

762 According to the results in this Figure S7b, we may filter the samples with
763 relatively small D_{COT} to further improve the accuracy of CBH retrieval by the VIS+IR
764 model (see Table S1). Figure S7b shows that after filtering the samples with the D_{COT}
765 less than 1.6, the R increases from 0.895 to 0.922, implying a better performance of
766 CBH retrieval. According to the ranking of predictor importance (see Fig. S6 in the
767 supplementary document), we also conduct another sensitivity test on the BT
768 observed by H8/AHI IR Channel-14 (Cha14) at 11 μm , which plays an important role
769 in the IR-single model. Figure S7c shows that the BT values of H8/AHI Channel-14
770 ranges from 160 K to 316 K, and the samples with BT higher than 300 K show large
771 CBH errors. Similarly, by filtering the samples with BT higher than 281 K, we can get
772 a better IR-single model algorithm for retrieving high-quality CBH (see Table S2 in
773 the supplementary document). Figure S7d also proves that the R value increases from
774 0.868 to 0.911.

775

776

777

778

779

780

781

782

783

784

785

786 **Reference**

787 Aydin, K. and Singh, J.: Cloud Ice Crystal Classification Using a 95-GHz Polarimetric Radar, *Journal of*
788 *Atmospheric and Oceanic Technology*, 21, 1679–1688, <https://doi.org/10.1175/JTECH1671.1>, 2004.

789 Baker, N.: Joint Polar Satellite System (JPSS) VIIRS Cloud Base Height Algorithm Theoretical Basis
790 Document (ATBD), 2011.

791 Baum, B., Menzel, W. P., Frey, R., Tobin, D., Holz, R., and Ackerman, S.: MODIS cloud top property
792 refinements for Collection 6, *Journal of Applied Meteorology and Climatology*, 51, 1145-1163,
793 10.1175/JAMC-D-11-0203.1, 2012.

794 Bessho, K., Date, K., Hayashi, M., Ikeda, A., Imai, T., Inoue, H., Kumagai, Y., Miyakawa, T., Murata, H.,
795 Ohno, T., Okuyama, A., Oyama, R., Sasaki, Y., Shimazu, Y., Shimoji, K., Sumida, Y., Suzuki, M., Taniguchi,
796 H., Tsuchiyama, H., Uesawa, D., Yokota, H., and Yoshida, R.: An introduction to Himawari-8/9—Japan's
797 new-generation geostationary meteorological satellites, *Journal of the Meteorological Society of*
798 *Japan*, 94, 151-183, 10.2151/jmsj.2016-009, 2016.

799 Breiman, L.: Random forests, *Machine Learning*, 45, 5-32, 2001.

800 Ceccaldi, M., Delanoë, J., Hogan, R. J., Pounder, N. L., Protat, A., and Pelon, J.: From CloudSat-CALIPSO
801 to EarthCare: Evolution of the DARDAR cloud classification and its comparison to airborne radar-lidar
802 observations, *Journal of Geophysical Research: Atmospheres*, 118, 7962-7981, 10.1002/jgrd.50579,
803 2013.

804 Forsythe, J. M., Haar, T. H. V., and Reinke, D. L.: Cloud-Base height estimates using a combination of
805 Meteorological Satellite Imagery and Surface Reports, *Journal of Applied Meteorology and Climatology*,
806 39, 2336–2347, [https://doi.org/10.1175/1520-0450\(2000\)039<2336:CBHEUA>2.0.CO;2](https://doi.org/10.1175/1520-0450(2000)039<2336:CBHEUA>2.0.CO;2), 2000.

807 Gregorutti, B., Michel, B., and Saint-Pierre, P.: Correlation and variable importance in random forests,
808 *Statistics and Computing*, 27, 659-678, 10.1007/s11222-016-9646-1, 2017.

809 Håkansson, N., Adok, C., Thoss, A., Scheirer, R., and Hörnquist, S.: Neural network cloud top pressure
810 and height for MODIS, *Atmospheric Measurement Techniques*, 11, 3177–3196,
811 10.5194/amt-11-3177-2018, 2018.

812 Hansen, B.: A Fuzzy Logic-Based Analog Forecasting System for Ceiling and Visibility, *Weather and*
813 *Forecasting*, 22, 1319-1330, 10.1175/2007waf2006017.1, 2007.

814 Hartmann, D. L. and Larson, K.: An important constraint on tropical cloud - climate feedback, *Geophys*
815 *Res Lett*, 29, 12-11-12-14, 10.1029/2002gl015835, 2002.

816 Heidinger, A. and Pavolonis, M.: Gazing at cirrus clouds for 25 years through a split window, part 1:
817 *Methodology*, *Journal of Applied Meteorology and Climatology*, 48, 1110-1116,
818 10.1175/2008JAMC1882.1, 2009.

819 Heidinger, A. K., Bearson, N., Foster, M. J., Li, Y., Wanzong, S., Ackerman, S., Holz, R. E., Platnick, S., and
820 Meyer, K.: Using sounder data to improve cirrus cloud height estimation from satellite imagers,
821 *Journal of Atmospheric and Oceanic Technology*, 36, 1331-1342, 10.1175/jtech-d-18-0079.1, 2019.

822 Heymsfield, A. J., Bansemer, A., Matrosov, S., and Tian, L.: The 94-GHz radar dim band: Relevance to
823 ice cloud properties and CloudSat, *Geophys. Res. Lett.*, 35, 10.1029/2007GL031361, 2008.

824 Hirsch, E., Agassi, E., and Koren, I.: A novel technique for extracting clouds base height using ground
825 based imaging, *Atmospheric Measurement Techniques*, 4, 117-130, 10.5194/amt-4-117-2011, 2011.

826 Hunt, W. H., Winker, D. M., Vaughan, M. A., Powell, K. A., Lucker, P. L., and Weimer, C.: CALIPSO lidar
827 description and performance assessment, *J. Atmos. Oceanic. Technol.*, 26, 2009.

828 Huo, J., Bi, Y., Lü, D., and Duan, S.: Cloud Classification and Distribution of Cloud Types in Beijing Using
829 Ka-Band Radar Data, *Advances in Atmospheric Sciences*, 36, 793-803, 10.1007/s00376-019-8272-1,

830 2019.

831 Hutchison, K., Wong, E., and Ou, S. C.: Cloud base heights retrieved during night-time conditions with
832 MODIS data, *Int J Remote Sens*, 27, 2847-2862, 10.1080/01431160500296800, 2006.

833 Hutchison, K. D.: The retrieval of cloud base heights from MODIS and three-dimensional cloud fields
834 from NASA's EOS Aqua mission, *Int J Remote Sens*, 23, 5249-5265, 10.1080/01431160110117391,
835 2002.

836 Iwabuchi, H., Putri, N. S., Saito, M., Tokoro, Y., Sekiguchi, M., Yang, P., and Baum, B. A.: Cloud Property
837 Retrieval from Multiband Infrared Measurements by Himawari-8, *Journal of the Meteorological
838 Society of Japan. Ser. II*, 96B, 27-42, 10.2151/jmsj.2018-001, 2018.

839 Kalnay, E., Kanamitsu, M., Kistler, R., Collins, W., Deaven, D., Gandin, L., Iredell, M., Saha, S., White, G.,
840 Woollen, J., Zhu, Y., Leetmaa, A., Reynolds, R., Chelliah, M., Ebisuzaki, W., W Higgins, J., Janowiak, J., Mo,
841 K. C., Ropelewski, C., and Wang, J.: The NCEP NCAR 40-Year Reanalysis Project, 1996.

842 Kühnlein, M., Appelhans, T., Thies, B., and Nauß, T.: Precipitation Estimates from MSG SEVIRI Daytime,
843 Nighttime, and Twilight Data with Random Forests, *Journal of Applied Meteorology and Climatology*,
844 53, 2457-2480, 10.1175/jamc-d-14-0082.1, 2014.

845 Letu, H., Nagao, T. M., Nakajima, T. Y., Riedi, J., Ishimoto, H., Baran, A. J., Shang, H., Sekiguchi, M., and
846 Kikuchi, M.: Ice cloud properties from Himawari-8/AHI next-generation geostationary satellite:
847 Capability of the AHI to monitor the DC cloud generation process, *IEEE Transactions on Geoscience
848 and Remote Sensing*, 57, 3229-3239, 10.1109/tgrs.2018.2882803, 2019.

849 Li, Y., Yi, B., and Min, M.: Diurnal variations of cloud optical properties during day-time over China
850 based on Himawari-8 satellite retrievals, *Atmospheric Environment*, 277, 119065,
851 10.1016/j.atmosenv.2022.119065, 2022.

852 Liang, Y., Min, M., Yu, Y., Wang, X., and Xia, P.: Assessing diurnal cycle of cloud covers of Fengyun-4A
853 geostationary satellite based on the manual observation data in China, *IEEE Transactions on
854 Geoscience and Remote Sensing*, 61, 10.1109/TGRS.2023.3256365, 2023.

855 Lin, H., Li, Z., Li, J., Zhang, F., Min, M., and Menzel, W. P.: Estimate of daytime single-layer cloud base
856 height from Advanced Baseline Imager measurements, *Remote Sensing of Environment*, 274, 112970,
857 10.1016/j.rse.2022.112970, 2022.

858 Lu, X., Mao, F., Rosenfeld, D., Zhu, Y., Pan, Z., and Gong, W.: Satellite retrieval of cloud base height and
859 geometric thickness of low-level cloud based on CALIPSO, *Atmospheric Chemistry and Physics*, 21,
860 10.5194/acp-21-11979-2021, 2021.

861 Meerkötter, R. and Bugliaro, L.: Diurnal evolution of cloud base heights in convective cloud fields from
862 MSG/SEVIRI data *Atmospheric Chemistry and Physics*, 9, 1767-1778, 10.5194/acp-9-1767-2009,
863 2009.

864 Miller, R. M., Rauber, R. M., Girolamo, L. D., Rilloraza, M., Fu, D., McFarquhar, G. M., Nesbitt, S. W.,
865 Ziemb, L. D., Woods, S., and Thornhill, K. L.: Influence of natural and anthropogenic aerosols on cloud
866 base droplet size distributions in clouds over the South China Sea and West Pacific, *Atmospheric
867 Chemistry and Physics*, 23, 8959-8977, 10.5194/acp-23-8959-2023, 2023.

868 Miller, S. D., Rogers, M. A., Haynes, J. M., Sengupta, M., and Heidinger, A. K.: Short-term solar
869 irradiance forecasting via satellite/model coupling, *Solar Energy*, 168, 102-117,
870 10.1016/j.solener.2017.11.049, 2018.

871 Min, M. and Zhang, Z.: On the influence of cloud fraction diurnal cycle and sub-grid cloud optical
872 thickness variability on all-sky direct aerosol radiative forcing, *Journal of Quantitative Spectroscopy
873 and Radiative Transfer*, 142, 25-36, 10.1016/j.jqsrt.2014.03.014., 2014.

874 Min, M., Li, J., Wang, F., Liu, Z., and Menzel, W. P.: Retrieval of cloud top properties from advanced
875 geostationary satellite imager measurements based on machine learning algorithms, *Remote Sensing*
876 of Environment

877 239, 111616, 10.1016/j.rse.2019.111616 2020.

878 Min, M., Chen, B., Xu, N., He, X., Wei, X., and Wang, M.: Nonnegligible diurnal and long-term variation
879 characteristics of the calibration biases in Fengyun-4A/AGRI infrared channels based on the oceanic
880 drifter data, *IEEE Transactions on Geoscience and Remote Sensing*, 60, 1-15,
881 10.1109/TGRS.2022.3160450, 2022.

882 Min, M., Wu, C., Li, C., Liu, H., Xu, N., Wu, X., Chen, L., Wang, F., Sun, F., Qin, D., Wang, X., Li, B., Zheng,
883 Z., Cao, G., and Dong, L.: Developing the science product algorithm testbed for Chinese
884 next-generation geostationary meteorological satellites: FengYun-4 series, *Journal of Meteorological
Research*, 31, 708-719, 10.1007/s13351-017-6161-z, 2017.

885 Noh, Y.-J., Miller, S. D., Seaman, C. J., Haynes, J. M., Li, Y., Heidinger, A. K., and Kulie, M. S.: Enterprise
886 AWG Cloud Base Algorithm (ACBA), 2022.

887 Noh, Y.-J., Forsythe, J. M., Miller, S. D., Seaman, C. J., Li, Y., Heidinger, A. K., Lindsey, D. T., Rogers, M. A.,
888 and Partain, P. T.: Cloud-base height estimation from VIIRS. Part II: A statistical algorithm based on
889 A-Train satellite data, *Journal of Atmospheric and Oceanic Technology*, 34, 585-598,
890 10.1175/JTECH-D-16-0110.1, 2017.

891 Omar, A., Winker, D., Kittaka, C., Vaughan, M., Liu, Z., Hu, Y., Trepte, C., Rogers, R., Ferrare, R., Kuehn,
892 R., and Hostetler, C.: The CALIPSO automated aerosol classification and lidar ratio selection algorithm,
893 *J. Atmos. Oceanic Technol.*, 26, 1994-2014, 10.1175/2009JTECHA1231, 2009.

894 Platnick, S., Meyer, K. G., King, M. D., Wind, G., Amarasinghe, N., Marchant, B., Arnold, G. T., Zhang, Z.,
895 Hubanks, P. A., Holz, R. E., Yang, P., Ridgway, W. L., and Riedi, J.: The MODIS cloud optical and
896 microphysical products: Collection 6 updates and examples from Terra and Aqua, *IEEE Trans Geosci
897 Remote Sens*, 55, 502-525, 10.1109/TGRS.2016.2610522, 2017.

898 Rosenfeld, D., Zheng, Y., Hashimshoni, E., Pohlker, M. L., Jefferson, A., Pohlker, C., Yu, X., Zhu, Y., Liu, G.,
899 Yue, Z., Fischman, B., Li, Z., Giguzin, D., Goren, T., Artaxo, P., Barbosa, H. M., Poschl, U., and Andreae,
900 M. O.: Satellite retrieval of cloud condensation nuclei concentrations by using clouds as CCN chambers,
901 *Proc. Natl. Acad. Sci.*, 113, 5828-5834, 10.1073/pnas.1514044113, 2016.

902 Sassen, K. and Wang, Z.: Classifying clouds around the globe with the CloudSat radar: 1-year of results,
903 *Geophys. Res. Lett.*, 35, 1-5, doi:10.1029/2007GL032591, 2008.

904 Seaman, C. J., Noh, Y.-J., Miller, S. D., Heidinger, A. K., and Lindsey, D. T.: Cloud-base height estimation
905 from VIIRS. Part I: Operational algorithm validation against CloudSat, *Journal of Atmospheric and
906 Oceanic Technology*, 34, 567-583, 10.1175/jtech-d-16-0109.1, 2017.

907 Sharma, S., Vaishnav, R., Shukla, M. V., Kumar, P., Kumar, P., Thapliyal, P. K., Lal, S., and Acharya, Y. B.:
908 Evaluation of cloud base height measurements from Ceilometer CL31 and MODIS satellite over
909 Ahmedabad, India, *Atmospheric Measurement Techniques*, 9, 711-719, 10.5194/amt-9-711-2016,
910 2016.

911 Stephens, G. L., Vane, D. G., Boain, R. J., Mace, G. G., and Sassen, K.: The CloudSat mission and the
912 A-Train: A new dimension of space-based observations of clouds and precipitation, *Bull. Amer. Meteor.
913 Soc.*, 83, 1771-1790, 2002.

914 Stubenrauch, C. J., Rossow, W. B., Kinne, S., Ackerman, S., Cesana, G., Chepfer, H., Di Girolamo, L.,
915 Getzewich, B., Guignard, A., Heidinger, A., Maddux, B. C., Menzel, W. P., Minnis, P., Pearl, C., Platnick,
916 S., Poulsen, C., Riedi, J., Sun-Mack, S., Walther, A., Winker, D., Zeng, S., and Zhao, G.: Assessment of
917 global cloud datasets from satellites: project and database initiated by the GEWEX radiation panel,

918 Bulletin of the American Meteorological Society, 94, 1031-1049, 10.1175/bams-d-12-00117.1, 2013.

919 Su, T., Zheng, Y., and Li, Z.: Methodology to determine the coupling of continental clouds with surface
920 and boundary layer height under cloudy conditions from lidar and meteorological data, Atmospheric
921 Chemistry and Physics, 22, 1453-1466, 10.5194/acp-22-1453-2022, 2022.

922 Tan, Z., Huo, J., Ma, S., Han, D., Wang, X., Hu, S., and Yan, W.: Estimating cloud base height from
923 Himawari-8 based on a random forest algorithm, Int J Remote Sens, 42, 2485-2501,
924 10.1080/01431161.2020.1854891, 2020.

925 Thorsen, T. J., Fu, Q., and Comstock, J.: Comparison of the CALIPSO satellite and ground-based
926 observations of cirrus clouds at the ARM TWP sites, Journal of Geophysical Research: Atmospheres,
927 116, 10.1029/2011jd015970, 2011.

928 Viúdez-Mora, A., Costa-Surós, M., Calbó, J., and González, J. A.: Modeling atmospheric longwave
929 radiation at the surface during overcast skies: The role of cloud base height, Journal of Geophysical
930 Research: Atmospheres, 120, 199-214, 10.1002/2014jd022310, 2015.

931 Wang, F., Min, M., Xu, N., Liu, C., Wang, Z., and Zhu, L.: Effects of linear calibration errors at low
932 temperature end of thermal infrared band: Lesson from failures in cloud top property retrieval of
933 FengYun-4A geostationary satellite, IEEE Transactions on Geoscience and Remote Sensing, 60,
934 5001511, 10.1109/TGRS.2022.3140348, 2022.

935 Wang, T., Shi, J., Ma, Y., Letu, H., and Li, X.: All-sky longwave downward radiation from satellite
936 measurements: General parameterizations based on LST, column water vapor and cloud top
937 temperature, ISPRS Journal of Photogrammetry and Remote Sensing, 161, 52-60,
938 10.1016/j.isprsjprs.2020.01.011, 2020.

939 Wang, X., Min, M., Wang, F., Guo, J., Li, B., and Tang, S.: Intercomparisons of cloud mask product
940 among Fengyun-4A, Himawari-8 and MODIS, IEEE Transactions on Geoscience and Remote Sensing, 57,
941 8827-8839, 10.1109/TGRS.2019.2923247 2019.

942 Wang, Z., Vane, D., Stephens, G., Reinke, D., and TBD: Level 2 combined radar and lidar cloud scenario
943 classification product process description and interface control document, 2012.

944 Warren, S. G. and Eastman, R.: Diurnal Cycles of Cumulus, Cumulonimbus, Stratus, Stratocumulus, and
945 Fog from Surface Observations over Land and Ocean, J Climate, 27, 2386-2404,
946 10.1175/jcli-d-13-00352.1, 2014.

947 Winker, D. M., Vaughan, M. A., Omar, A., Hu, Y., Powell, K. A., Liu, Z., Hunt, W. H., and Young, S. A.:
948 Overview of the CALIPSO mission and CALIOP data processing algorithms, J. Atmos. Oceanic. Technol.,
949 26, 2310-2323, 10.1175/2009JTECHA1281.1, 2009.

950 Yang, J., Li, S., Gong, W., Min, Q., Mao, F., and Pan, Z.: A fast cloud geometrical thickness retrieval
951 algorithm for single-layer marine liquid clouds using OCO-2 oxygen A-band measurements, Remote
952 Sensing of Environment, 256, 10.1016/j.rse.2021.112305, 2021.

953 Young, S. A. and Vaughan, M. A.: The retrieval of profiles of particulate extinction from Cloud Aerosol
954 Lidar Infrared Pathfinder Satellite Observations (CALIPSO) data: Algorithm description, J. Atmos.
955 Oceanic. Technol., 26, 1105-1119, 10.1175/2008JTECHA1221.1, 2009.

956 Zhang, Y., Zhang, L., Guo, J., Feng, J., Cao, L., Wang, Y., Zhou, Q., Li, L., Li, B., Xu, H., Liu, L., An, N., and
957 Liu, H.: Climatology of cloud-base height from long-term radiosonde measurements in China,
958 Advances in Atmospheric Sciences, 35, 158-168, 10.1007/s00376-017-7096-0, 2018.

959 Zheng, Y. and Rosenfeld, D.: Linear relation between convective cloud base height and updrafts and
960 application to satellite retrievals, Geophys Res Lett, 42, 6485-6491, 10.1002/2015gl064809, 2015.

961 Zheng, Y., Sakradzija, M., Lee, S.-S., and Li, Z.: Theoretical Understanding of the Linear Relationship

962 between Convective Updrafts and Cloud-Base Height for Shallow Cumulus Clouds. Part II: Continental
963 Conditions, *J Atmos Sci*, 77, 1313-1328, 10.1175/jas-d-19-0301.1, 2020.

964 Zhou, Q., Zhang, Y., Li, B., Li, L., Feng, J., Jia, S., Lv, S., Tao, F., and Guo, J.: Cloud-base and cloud-top
965 heights determined from a ground-based cloud radar in Beijing, China, *Atmospheric Environment*, 201,
966 381-390, 10.1016/j.atmosenv.2019.01.012, 2019.

967 Zhou, R., Pan, X., Xiaohu, Z., Na, X., and Min, M.: Research progress and prospects of atmospheric
968 motion vector based on meteorological satellite images, *Reviews of Geophysics and Planetary Physics*
969 (In Chinese), 55, 184-194, 10.19975/j.dqyxx.2022-077, 2024.

970 Zhu, Y., Rosenfeld, D., Yu, X., Liu, G., Dai, J., and Xu, X.: Satellite retrieval of convective cloud base
971 temperature based on the NPP/VIIRS Imager, *Geophys Res Lett*, 41, 1308-1313,
972 10.1002/2013gl058970, 2014.

973

974

975

976

977

978

979

980

981

982

983

984

985

986

987

988

989

990

991

992

993

994

995

996

997

998

999

Tables and Figures

1000

1001 **Table 1.** Predictand and predictor variables for both visible (VIS)+infrared (IR) model
 1002 and IR-single regression model training, which are divided according to the different
 1003 predictor variables from satellite and NWP data

Predictand	IR-single model input	VIS+IR model input
Predictor [satellite measurements]	BT(3.9 μ m), BT(6.2 μ m), BT(6.9 μ m), BT(7.3 μ m), BT(8.6 μ m), BT(9.6 μ m), BT(10.4 μ m), BT(11.2 μ m), BT(12.4 μ m), BT(13.3 μ m), BTD(11.2–12.4 μ m), BTD(11.2– 13.3 μ m) [Unit = K], Air Mass (1/cos(VZA)), View azimuth angles [Unit = degree], Cloud top height from H8/AHI [unit: m], Cloud top temperature from H8/AHI [unit: K]	BT(3.9 μ m), BT(6.2 μ m), BT(6.9 μ m), BT(7.3 μ m), BT(8.6 μ m), BT(9.6 μ m), BT(10.4 μ m), BT(11.2 μ m), BT(12.4 μ m), BT(13.3 μ m), BTD(11.2–12.4 μ m), BTD(11.2– 13.3 μ m) [Unit = K], Air Mass(1/cos(VZA)), Air Mass(1/cos(SZA)), View/Solar Azimuth angles [Unit = degree], Cloud top height from H8/AHI [unit: m], Cloud top temperature from H8/AHI [unit: K] Ref(0.47 μ m), Ref(0.51 μ m), Ref(0.64 μ m), Ref(0.86 μ m), Ref(1.64 μ m), Ref(2.25 μ m)
Predictor [GFS NWP]	Altitude profile (from surface to about 21 km, 67 layers) [unit: m], Temperature profile (from surface to about 21 km, 67 layers) [unit: K], Relative humidity profile (from surface to about 21 km, 67 layers) [unit: %], Total precipitable water, Surface temperature [unit: K]	Altitude profile (from surface to about 21 km, 67 layers) [unit: m], Temperature profile (from surface to about 21 km, 67 layers) [unit: K], Relative humidity profile (from surface to about 21 km, 67 layers) [unit: %], Total precipitable water, Surface temperature [unit: K]
Predictor [other]	Surface elevation [unit: m]	Surface elevation [unit: m]

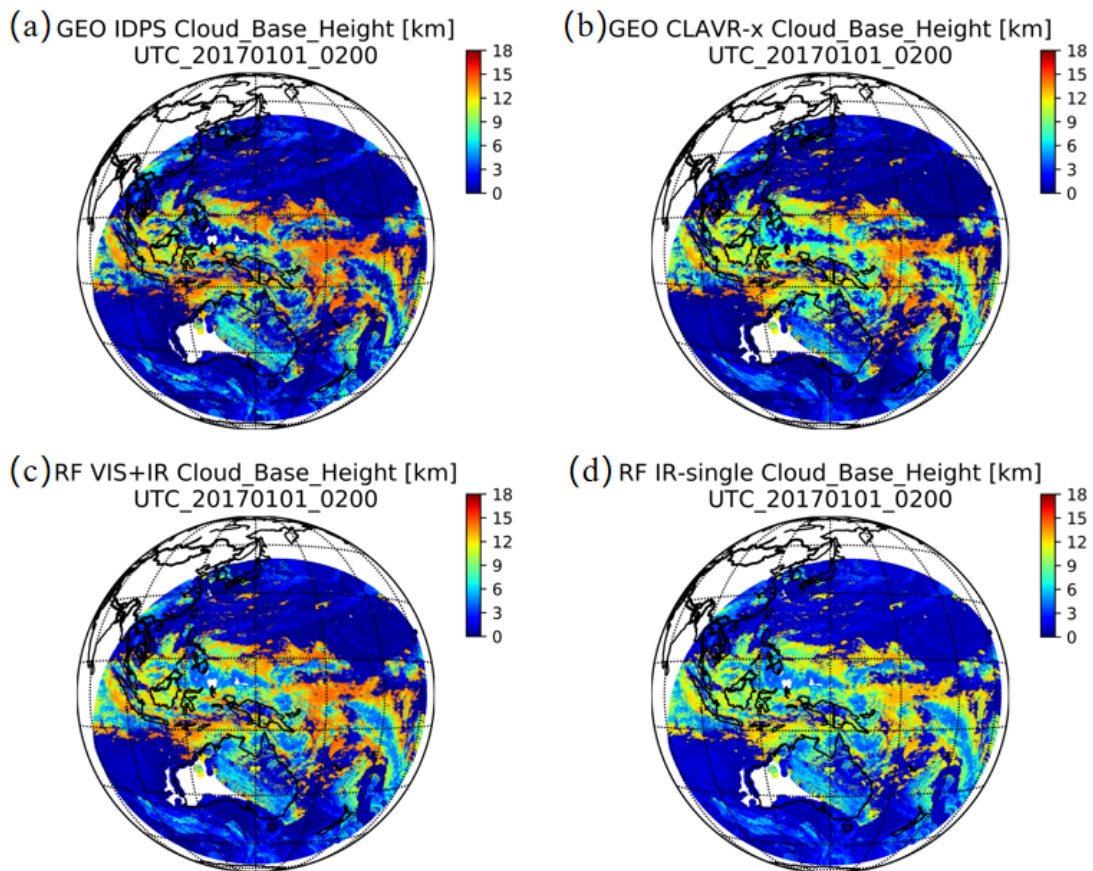
1004 Notes: VZA = view zenith angle [unit: degree]; SZA = solar zenith angle [unit:
 1005 degree]

1006

1007

1008

1009
1010
1011
1012
1013
1014
1015
1016
1017
1018



1019

1020 **Figure 1.** Comparison of full disk CBH results retrieved by the four independent
1021 algorithms at 02:00 UTC on January 1, 2017. (a) GEO IDPS algorithm, (b) GEO
1022 Clouds from AVHRR Extended (CLAVR-x) algorithm, (c) ML-based (RF, random
1023 forest) VIS+IR algorithm and (d) ML-based (RF) IR-single algorithm.

1024

1025

1026

1027

1028

1029

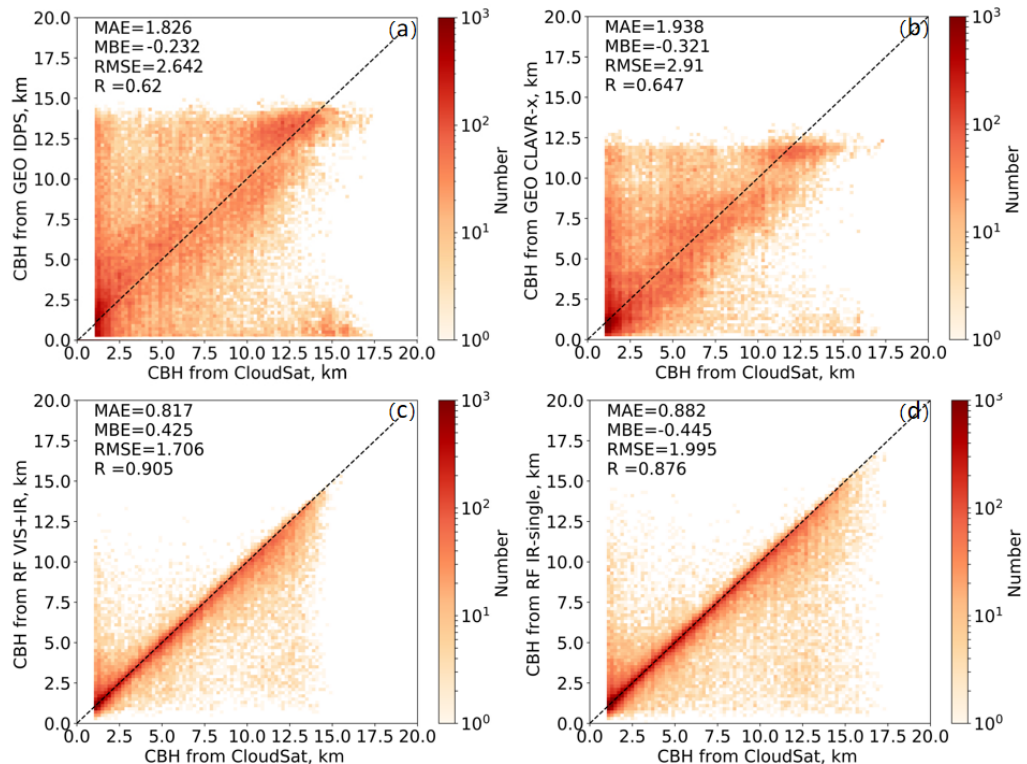
1030

1031

1032

1033

1034



1035

1036

1037

1038

1039

1040

1041

1042

1043

1044

1045

1046

1047

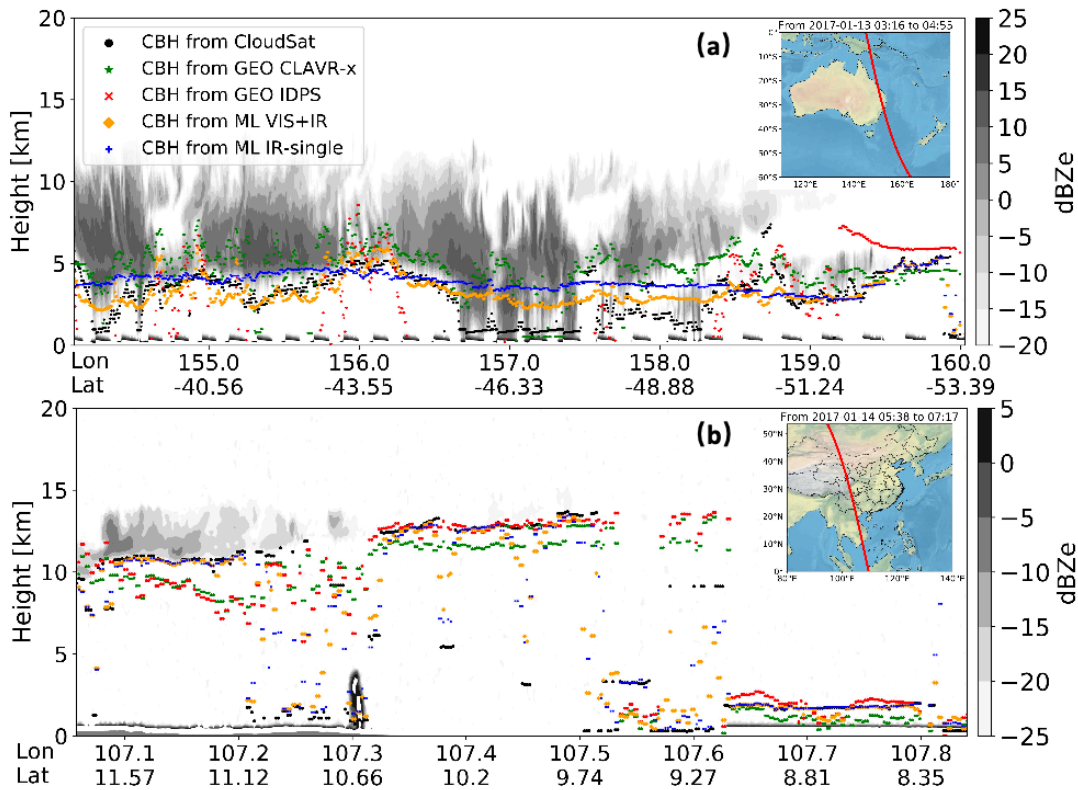
1048

1049

1050

Figure 2. Density distributions of CBHs retrieved from (a) GEO IDPS, (b) GEO CLAVR-x, (c) VIS+IR and (d) IR-single algorithms compared with the CBHs from the joint CloudSat/CALIPSO product (taken as true values) in 2017 for both single and multilayer clouds. The mean absolute error (MAE), mean bias error (MBE), root mean square error (RMSE) and R are listed in each subfigure where the difference exceeds the 95% significance level ($p < 0.05$) according to the Pearson's χ^2 test.

1051
1052
1053
1054
1055

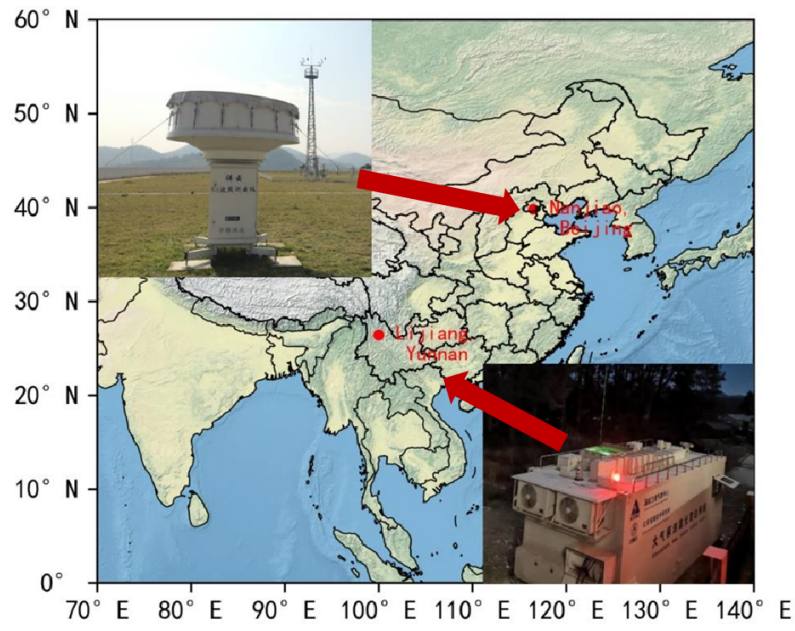


1056

1057 **Figure 3.** Inter-comparisons of CBH products retrieved by CloudSat (red solid circle),
1058 the GEO IDPS algorithm (blue solid circle), the GEO CLAVR-x (green solid circle),
1059 the ML-based VIS+IR model algorithm (orange solid circle), and the ML-based
1060 IR-single model algorithm (pink solid circle) at (a) 03:16–04:55 UTC on January 13,
1061 2017 (a) and (b) 05:38–07:17 UTC on January 14, 2017. The black and gray colormap
1062 represents the matched CloudSat radar reflectivity.

1063
1064
1065
1066
1067
1068
1069

1070
1071
1072
1073
1074
1075



1076

Figure 4. Geographical locations and photos of lidar and cloud radar at Yunnan Lijiang and Beijing Nanjiao stations.

1079
1080
1081
1082
1083
1084
1085
1086
1087
1088
1089
1090
1091
1092

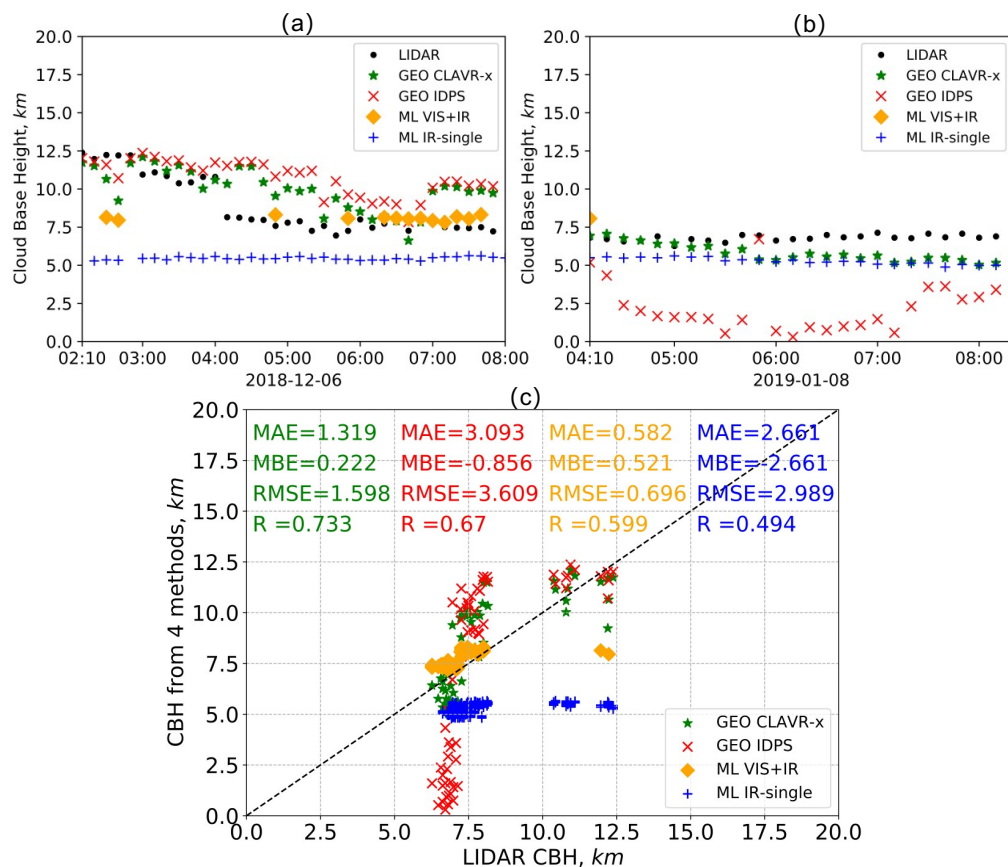
1093

1094

1095

1096

1097



1098

1099 **Figure 5.** Comparisons of the CBHs from the ground-based lidar measurements
1100 (black solid circle) at Yunnan Lijiang station and the four GEO satellite retrieval
1101 algorithms, namely the GEO IDPS (red cross symbol), the GEO CLAVR-x (green
1102 solid asterisk), the ML-based VIS+IR model (orange solid diamond) and the
1103 ML-based IR-single model (blue plus sign) algorithms. Figure 5a and 5b show the
1104 time series of CBHs from lidar and the four GEO satellite retrieval algorithms on
1105 December 6, 2018 and January 8, 2019, respectively. Fig 5c shows the scatterplots of
1106 CBH samples from the lidar measurements and the four retrieval algorithms.

1107

1108

1109

1110

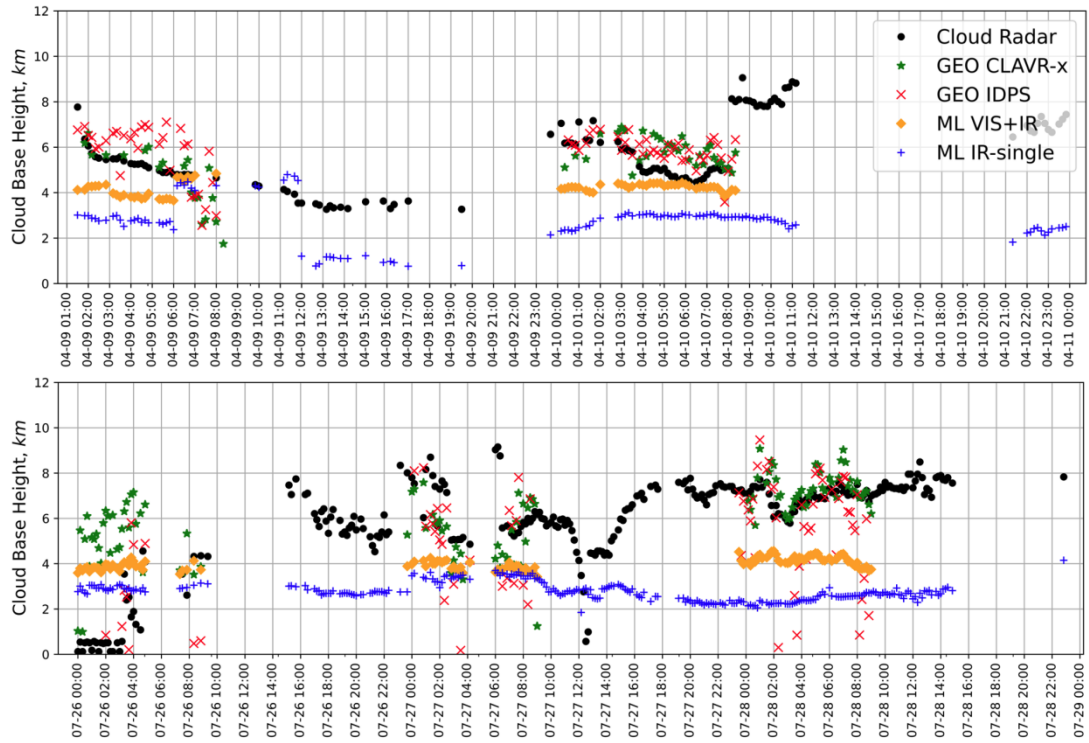
1111

1112

1113

1114

1115



1116

1117 **Figure 6.** Same as Figure 5, but for the CBH sample results from the cloud radar at
1118 Beijing Nanjiao station (black solid circle) on April 9–10, 2017 (top panel) and July
1119 26–28, 2017 (bottom panel).

1120

1121

1122

1123

1124

1125

1126

1127

1128

1129

1130

1131

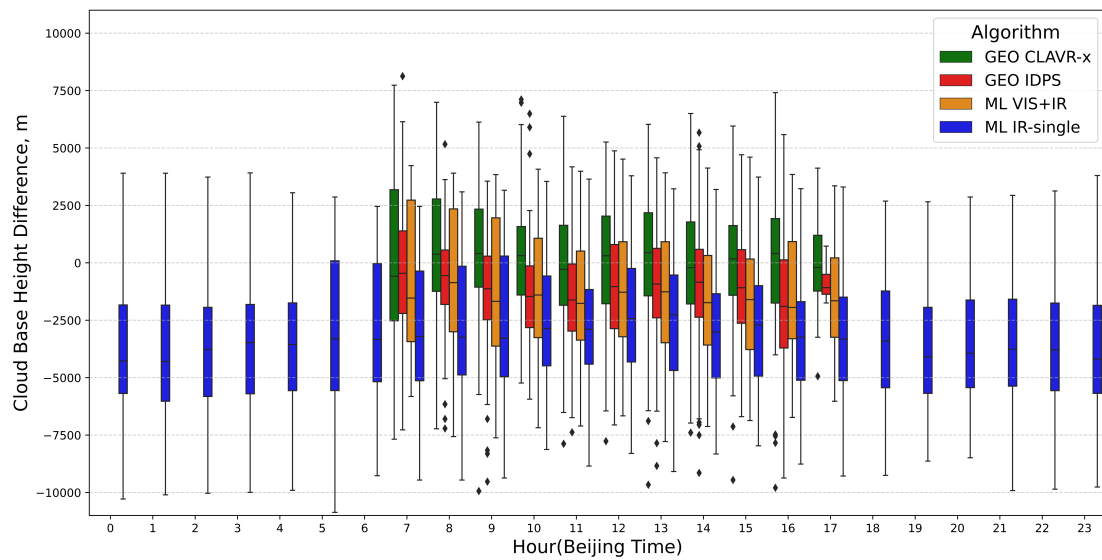
1132

1133

1134

1135

1136



1137

Figure 7. Box plots of the hourly CBH errors of four GEO satellite retrieval algorithms (GEO IDPS, GEO CLAVR-x, ML-based VIS+IR and ML-based IR-single) relative to the CBHs from the cloud radar at Beijing Nanjiao station in 2017. The box symbols signify the 25th, 50th and 75th percentiles of errors. The most extreme sample points between the 75th and outlier, and the 25th percentiles and outliers are marked as whiskers and diamonds, respectively. Except for the period between 7 and 17 (local time), the three algorithms of GEO CLAVR-x, GEO IDPS, and ML VIS+IR are unavailable due to the lack of reflected solar radiance measurements.

1146

1147

1148

1149

1150

1151

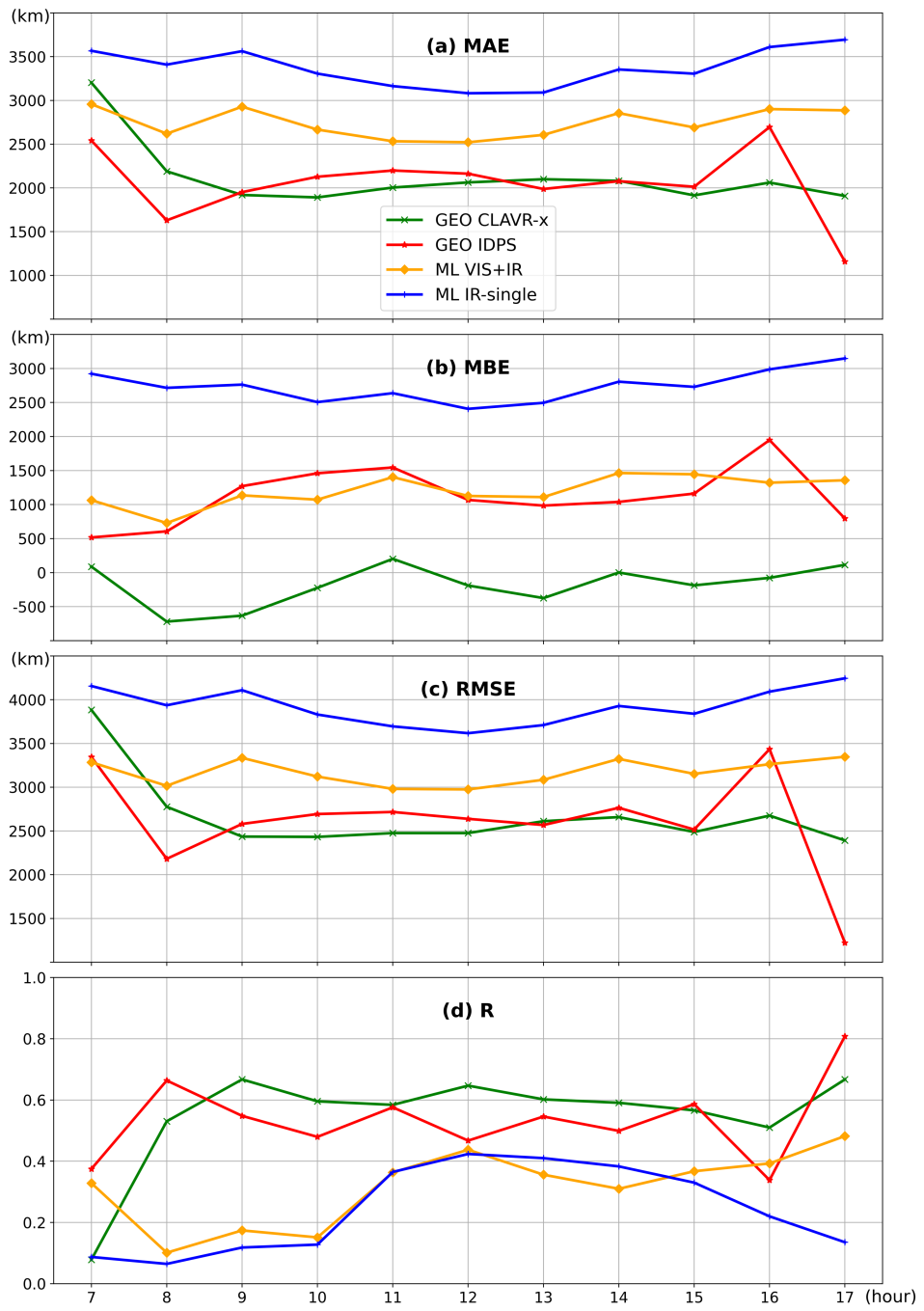
1152

1153

1154

1155

1156



1157

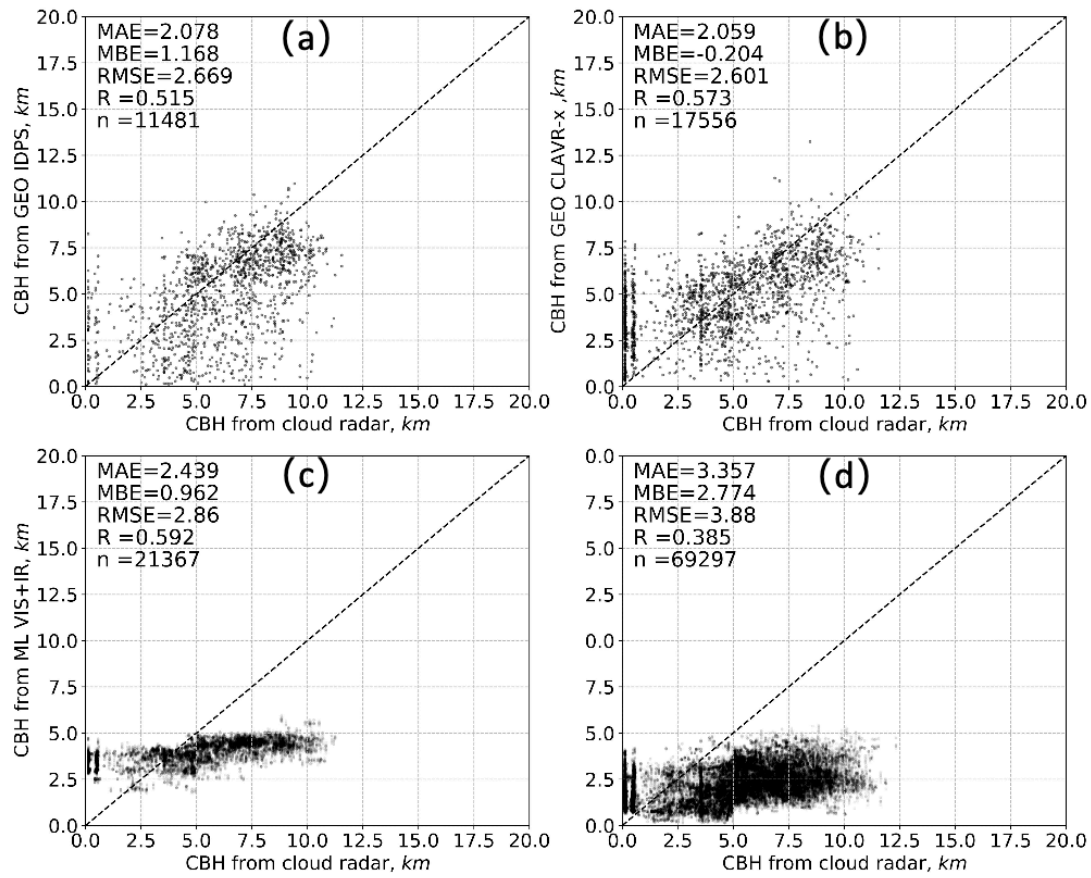
1158 **Figure 8.** Comparisons of hourly (a) MAE, (b) MBE, (c) RMSE, and (d) R of CBH
 1159 (relative to the CBHs from the cloud radar at Beijing Nanjiao station) from 07 to 17
 1160 (local time) between four retrieval algorithms (GEO IDPS, GEO CLAVR-x,
 1161 ML-based VIS+IR and ML-based IR-single) in 2017.

1162

1163

1164

1165



1166

1167 **Figure 9.** Comparisons between the CBHs from the cloud radar at Beijing Nanjiao
1168 station and the matched CBHs from the four retrieval algorithms (GEO IDPS, GEO
1169 CLAVR-x, ML-based VIS+IR and ML-based IR-single) in 2017.

1170

1171

1172

1173

1174

1175